Collisional angular momentum depolarization of OH(A) and NO(A) by Ar: A comparison of mechanisms.

M. Brouard,[1, a)] H. Chadwick,[1] Y.-P. Chang,[1] C. J. Eyles,[1] F. J. Aoiz,[2, b)] and J. Kłos[3, c)]

[1)] *The Department of Chemistry, University of Oxford, The Physical and Theoretical Chemistry Laboratory, South Parks Road, Oxford, OX1 3QZ, United Kingdom.*

[2)] *Departamento de Química Física, Facultad de Química, Universidad Complutense, 28040 Madrid, Spain*

[3)] *Department of Chemistry and Biochemistry, University of Maryland, College Park, MD, 20742, USA*

(Dated: 21 July 2011)

This paper discusses the contrasting mechanisms of collisional angular momentum depolarization of OH($A\,^2\Sigma^+$) and NO($A\,^2\Sigma^+$) by Ar. New experimental results are presented for the collisional depolarization of OH(A) + Ar under both thermal and superthermal collision conditions, including cross sections for loss of both angular momentum orientation and alignment. Previous work on the two systems is summarized. It is shown that NO(A) + Ar depolarization is dominated by impulsive events, in which the projection of the angular momentum, $\boldsymbol{j}$, along the kinematic apse, $\boldsymbol{a}$, is nearly conserved, and in which the majority of the trajectories can be described as 'nearside'. By contrast, at the relatively low collision energies sampled at 300 K, OH(A) + Ar depolarization is dominated by attractive collisions, which show a preponderance of 'farside' trajectories. There is also evidence for very long-lived, complex type trajectories, in which OH(A) and Ar orbit each other for several rotational periods prior to separation. Nevertheless, there is still a clear preference for conservation of the projection of $\boldsymbol{j}$ along the kinematic apse for both elastic and inelastic collisions. Experimental and theoretical results reveal that, as the collision energy is raised, the depolarization of OH(A) by Ar becomes more impulsive-like in nature.

[a)] Electronic mail: mark.brouard@chem.ox.ac.uk

[b)] Electronic mail: aoiz@quim.ucm.es

[c)] Electronic mail: jklos@umd.edu

I. INTRODUCTION

There has been considerable recent interest in the study of collisional angular momentum depolarization in elastic and inelastic scattering[1–19]. This work has generally focussed on the collisions of simple open shell molecules with a range of collision partners. Such studies are of interest as they provide fundamental insight into the dynamics of elastic and inelastic scattering, and the role that analysis of vector correlations involving the initial and final angular momenta, $\boldsymbol{j}$ and $\boldsymbol{j}'$, can play in illuminating these dynamics.

The main emphasis of the current paper is a comparison of the mechanism of collisional angular momentum depolarization of NO(A) and OH(A) by Ar. Under thermal conditions, the depolarization of OH(A) by Ar is very efficient compared to rotational energy transfer (RET)[2–4], whereas for NO(A) + Ar it is relatively inefficient[6]. Recent theoretical work by Dagdigian and Alexander on the collisional elastic depolarization of OH(X) with Ar[16] and He[17], and NO(X) + Ar[18] at 300 K, which has a potential energy surface (PES) with a well-depth of $\sim$100 cm^{-1}, comparable to that of NO(A) + Ar, has shown that elastic depolarization is brought about by collisions that probe impact parameters between the inner repulsive wall and the attractive well of the potential, as opposed to the longer range region. This complements experimental studies by McKendrick and coworkers on collisional depolarization of OH(X) and CN(A) by a range of collision partners[7–15]. Rather different dynamical behaviour is anticipated in the case of OH(A) + Ar, which has a highly anisotropic PES, with well-depths of 1200 cm^{-1} and 1700 cm^{-1} for Ar approaching at the H- and O-ends of the radical, respectively[2].

In the following paper, new experimental collisional depolarization data are presented for OH(A) + Ar at both thermal and superthermal collision energies, and the way in which the distinctive dynamics of this system evolves with collision energy is explored in detail using in part the theoretical methods developed in the accompanying paper[20]. Although the majority of calculations presented here are classical, closed shell and open shell quantum mechanical (QM) calculations, also presented in the current paper, suggest that the classical approach provides a realistic description of the collision dynamics for the systems in question.

The outline of the paper is as follows. Section II first outlines the quasi-classical trajectory (QCT) and QM methods employed. It also describes briefly the experimental procedures, and the methods used to analyze the Zeeman quantum beats. The results from the

experiments and the quasi-classical trajectory calculations are presented and discussed in section III. In section IV a comparison of the mechanisms of collisional depolarization of NO(A) and OH(A) by Ar is presented, work which builds heavily on the QCT theoretical machinery developed in the accompanying paper[20]. The new experimental data on the collisional depolarization of OH(A) by Ar obtained under both thermal and superthermal conditions, in comparison to previously published 300 K data, are shown to provide an important indicator of the long range nature of the depolarization process. The final section summarizes our principal conclusions.

II. METHOD

A. Calculations

1. QCT Method

Full details of the QCT methods employed are described in the accompanying paper[20] and are not repeated here. Batches of approximately 1×10^5 trajectories were run for several initial N states at fixed collision energies of 0.039 eV, 0.76 eV, and 1.25 eV for OH(A) + Ar and 0.039 eV for NO(A) + Ar. The energy 0.039 eV corresponds to the mean thermal collision energy at 300 K, while 0.76 eV and 1.25 eV were chosen as representative values of the mean collision energies sampled in the superthermal experiments using 248 nm and 193 nm photolysis of H_2O_2 as the OH source, respectively. Since the potential energy surfaces for OH(A)-Ar[2] and NO(A)-Ar[21] have only been calculated using the fixed equilibrium bond lengths of the radicals, the method of Lagrange multipliers was used to force rigid rotor behavior during the integration of the classical equations of motion. For further details of the calculations we refer to the preceding paper[20].

Batches of approximately 3×10^5 trajectories were also run for OH(A) + Ar in which the collision energy was randomly and uniformly varied between 5×10^{-3} eV and 2.5 eV for each trajectory. From these trajectories at variable energy, collision energy dependent cross sections and polarization parameters, $\sigma_{NN'}(E_{\rm coll})$ and $a^{(k)}(N, N'; E_{\rm coll})$, were determined using methods described previously[2,4,22,23]. From these data, the dependence of the depolarization cross sections on collision energy, $\sigma^{(k)}(E_{\rm coll})$, was calculated. QCT calculations were also performed for $N = 5$ to determine the effect that the PES and radical mass combination

had on the mechanism of depolarization. Approximately 10^5 trajectories were run using the NO(A)–Ar masses on the OH(A)–Ar PES (*i.e.* changing the mass of the H from 1 u to 14 u) and the OH(A)–Ar masses on the NO(A)–Ar PES (*i.e.* changing the mass of the N from 14 u to 1 u) using a collision energy of 0.039 eV. These mass substitutions also imply a change in the position of the center-of-mass of the diatomic.

Note that the above treatment is appropriate for QCT calculations in which OH(A) + Ar and NO(A) + Ar are treated as closed shell systems. To compare with experimental results, QCT estimates of the 'open shell' spin-rotation level changing cross sections, and the associated polarization parameters, were obtained using the tensor opacity formalism described in detail previously in ref. 3, and in the accompanying paper[20]. As discussed at length in the accompanying paper (ref. 20), the QCT treatment of open shell Σ molecules is based upon the assumption that the electronic spin (as well as the nuclear spin) behaves as a spectator to the dynamics. This allows the calculation of the open shell RET, 'disorientation', and 'disalignment' cross sections using the QM expression for the state specific cross section and polarization parameters, Eqs. (20) and (23) of ref. 3, but with the tensor opacities evaluated using QCT methods (refs. 3 and 20).

Time delays and deflection functions have also been calculated in this work. The time delay is defined as the difference between the actual duration of the collision and the time that it would have taken if the potential had been switched off; that is,

$$\tau_{\rm del} = t_{\rm tot} - \frac{R_i}{v_{\rm r}} - \frac{R_f}{v'_{\rm r}}\,, \tag{1}$$

where $t_{\rm tot}$ is the actual duration of the trajectory, R_i and R_f are the initial (i) and final (f) distances between the atom and the center-of-mass of the diatom, and $v_{\rm r}$ and $v'_{\rm r}$ are the asymptotic initial and final velocities, respectively. Due to the presence of the repulsive potential, 'direct trajectories' have negative $\tau_{\rm del}$. Only those trajectories that result in the three atoms being temporarily trapped in the attractive potential give rise to positive time delays. Care should be exercised when comparing the time delays of trajectories ending in very different rotational states; endoergic collisions with considerable rotational excitation tend to have more negative $\tau_{\rm del}$ than those resulting from exoergic collisions. Deflection angles, χ, were determined by examining the three components of the final relative velocity with respect to the direction of the initial relative velocity. Orbiting trajectories with $\chi < -\pi$ were scarce but could be readily identified.

2. QM Method

Fully quantum close-coupling (CC) scattering calculations were performed for OH(A) + Ar using the *ab initio* PES of Kłos *et al.*[2] using the HIBRIDON suite of codes[24], which employs a hybrid propagator comprised of the log-derivative propagator by Manolopoulos[25,26] and the Airy propagator for the long range region. In the CC scattering calculations of the closed shell RET cross sections for $N = 5$ the propagation was performed from $3\,a_0$ to $90\,a_0$. The rotational basis of OH(A) included all states up to $N = 21$. The number of radial steps used in the propagator was 25, and partial waves up to $J = 360.5$ were used to converge the cross sections.

B. Experimental

1. General

The experimental procedures for determining depolarization cross sections from Zeeman quantum beat spectroscopy have been described previously[1,4], and only a brief summary will be given here. Translationally excited, superthermal OH(X) was generated by pulsed 248 nm or 193 nm photodissociation of hydrogen peroxide[27–36]. The H_2O_2 itself was flowed in a 50:50 mixture with water through the reaction chamber at a constant partial pressure of $\leq$2 mTorr. Electronically excited superthermal OH(A) radicals were obtained at a fixed pump-probe laser delay of 250 ns (see Section II B 2) by pulsed excitation of OH(X) using the A←X transition. For the thermal measurements a time delay of $\sim$10 μs was used. A counter-propagating laser beam geometry was employed. The levels $v' = 0$, $N' = 0$, 2, 5, 8 and 14 of the f_1 ($j = N + 1/2$) or f_2 ($j = N - 1/2$) spin-rotation manifold of OH(A) were excited using a variety of main and satellite P and R branch transitions (for the notation used in the following to label these transitions, see ref. 37).

The collider gas, Ar, flowed into the chamber through a separate inlet valve to allow experiments to be performed over a range of partial pressures, from around 100-1000 mTorr depending on conditions (see further below). The OH(A) spontaneous fluorescence was passed through a set of polarizing optics (see below), and the emission was then dispersed using a monochromator (in the case of orientation measurements), before being detected with a UV-sensitive photomultiplier. The fluorescence decay traces were recorded on a digital

oscilloscope and transferred to a PC for subsequent data acquisition and analysis. The response time of the system was determined to be $\lesssim$20 ns. The majority of the experiments were performed with broad-band Nd:YAG-pumped dye laser radiation, but some OH(X) laser induced fluorescence (LIF) spectra were obtained at higher Doppler-resolution using etalon-narrowed probe radiation of $\sim$0.08 cm^{-1} band-width in order to ascertain the extent of translational cooling on the timescale of the experiments.

A Glan-Taylor polarizer was used to improve the polarization of the frequency doubled dye laser radiation immediately prior to entering the reaction chamber, and the purity of the polarization was determined to be better than 95 % on exiting the chamber. In the case of alignment measurements, a photoelastic modulator was used to switch the probe laser linear polarization either 90° to the fluorescence detection direction or parallel to it on alternate laser shots. Only the data from the former geometry was used to analyze the collision loss of alignment (see Section II B 3), but the latter geometry, which in the absence of initial OH(X) polarization does not contain a quantum beat, was useful to obtain on-the-fly pure beat signals. The polarizer used for detection was aligned parallel to the probe laser propagation axis. The photolysis laser radiation was used without polarization. In the case of orientation measurements, the probe radiation was switched between left and right circularly polarized light on alternate laser shots using a photoelastic modulator. A quarter waveplate followed by a Glan-Taylor polarizer were placed in front of the entrance slits of the monochromator.

The experiments were performed in a uniform magnetic field of between 0 and 30 Gauss. The field was produced using a pair of matched Helmholtz coils, which were placed inside the reaction chamber, about 2.5 cm away from the interaction region. As in our previous work[1,4,6,7], the center of the reaction chamber was screened from external magnetic fields by μ-metal shielding. The field was checked using a Hall probe, but could also be determined from the Zeeman beat frequency, since the g_F values for OH(A) are known quite precisely[38–44]. For the alignment experiments, the axis of the magnetic field was aligned parallel to the fluorescence detection direction[1] while in the orientation experiments the field axis was directed perpendicular to the detection axis, and to the pump laser propagation direction[5].

2. Translational moderation of OH(A)

The OH(X) products from the 248 nm photodissociation of H_2O_2 are born translationally excited[1,27,29–36], with a narrow velocity distribution centred near 3850 m s^{-1} for $N'' = 9$. At 193 nm[28,45], the velocity of the $N'' = 10$ fragments is sharply centered around 4550 m s^{-1}. The superthermal experiments described here were performed in a similar fashion to those described previously when H_2O was used as the collider gas[1], in which the time-delay between the pump and probe lasers was fixed at 250 ns. On the timescales of the Zeeman beat experiments, translational moderation of both the ground and excited states of OH can potentially compete with the collisional depolarization process of interest. As previously[1], we have modeled the translational cooling of OH(X) based on measurements of Doppler-resolved LIF profiles as a function of pressure and time-delay between the pump and probe laser pulses. Given that translational moderation at the comparatively high collision energies of the present experiments is likely to be dominated by the repulsive wall of the potential, we believe the data also provide some indication of the extent of translational cooling that is likely to occur in the excited OH(A) state. The extent of cooling can be minimized to some extent by restricting the analyzed portion of the fluorescence decay to the first ∼500 ns, and the maximum Ar pressure employed to ∼400 mTorr.

Doppler-resolved LIF profiles, obtained over a range of delay-times, were compared with the results of a simple hard sphere model of the scattering dynamics, in which the angular distribution of the OH(X) products was assumed to be isotropic[1,46]. The model employed a single adjustable parameter, the effective moderation rate coefficient, k, defined as the product of the reactant relative velocity and the elastic scattering cross section, $k = v\sigma$, and the calculations described in the preceding section were used to provide a realistic estimate of these input moderation cross sections. The estimates of the moderation cross sections were between 10 Å^2 and 20 Å^2, depending on rotational quantum state, and the results of the model simulations using these estimates were found to be in good general agreement with the experimental Doppler profiles, and with previous work[46]. The optimized model was used to provide estimates of the mean relative velocity appropriate to the pressure and time-delay conditions used in each of the Zeeman quantum beat experiments. These relative velocities were then used to convert the experimentally measured rate coefficients into superthermal cross sections. Although these superthermal experiments are clearly not

conducted at a sharply defined collision energy, the simulations indicate that they do provide a simple means of determining the qualitative effect of raising the collision energy on the depolarization process.

The same simulation procedure, together with Doppler-resolved profile measurements, were used to verify that the OH(X) and OH(A) were translationally moderated down to 300 K under at the minimum pressures employed in the experiment (around 100 mTorr) and a time-delay of 10 μs. The fact that the OH and Ar have quite similar masses favors efficient translational moderation. So too does the effect of OH fly-out, since the most highly translationally excited OH(X) photofragments escape the interaction region on relatively short timescales ($\sim$1μs). Note that rotational thermalization takes place over longer timescales, but this is not a necessary condition for the experiments.

3. Zeeman quantum beats

The non-zero nuclear magnetic moment of the H-atom splits the rotational levels of OH(A) into a number of hyperfine components, characterized by the total angular momentum $\boldsymbol{F} = \boldsymbol{I} + \boldsymbol{j}$. The applied magnetic field lifts the degeneracy of each of these hyperfine sublevels (Zeeman splitting) resulting in $2F + 1$ components characterized by the quantum number M_F (the projection quantum number along the magnetic field direction). The dye laser employed in the present work has a pulse duration $\sim$5 ns, and hence quantum beats between levels split by more than $\sim$30 MHz will be unobservable (see further below). The energy splitting between the two hyperfine states of OH(A) with different F quantum numbers is of the order of several hundred MHz[47,48], hence only the beats between Zeeman components of the individual hyperfine sublevels are observed in the present work. It should be mentioned that the photodissociation of H_2O_2 at 248 nm and 193nm generates OH(X) photofragments with modest degrees of rotational alignment[27,28,32] and orientation[49]. Such OH(X) polarization could contribute to $k = 1, 2$ and high-order quantum beat signals. However, with unpolarized photolysis radiation, the degree of OH(X) polarization is very small[27,28,32,49] and any high-order contributions of OH(X) polarization to the OH(A) quantum beats were not observed, and could be safely neglected.

For alignment measurements, the fluorescence decays in the Zeeman quantum beat experiments obtained when the probe laser polarization was aligned perpendicular to the magnetic

field direction were fit using the following expression[38–40,44]:

$$I = A\,\mathrm{e}^{-k_\mathrm{p}t} \times \left[1 + \mathrm{e}^{-k_\mathrm{d}t} \sum_F C_F \cos\left(2\pi\alpha_F H t + \phi\right)\right] . \tag{2}$$

In this equation, H is the magnetic field strength, ϕ is the initial phase of the beat signal, defined by the probe laser and detector polarization geometries, and A and C_F are constants defining the total intensity and the relative beat amplitudes, respectively. In the analysis of Zeeman quantum beats, the latter vary only slightly with F for the levels probed in the present work. In the Hund's case (b) limit, appropriate to OH(A), the parameter α_F, which defines the beat frequency per unit applied field, can be written to a good approximation[38–40,44]

$$\alpha_F \simeq 2\,\frac{\mu_0}{h}\,g_F\,, \tag{3}$$

with

$$g_F = g_j \frac{F(F+1) + j(j+1) - I(I+1)}{2F(F+1)}\,, \tag{4}$$

and

$$g_j = g_\mathrm{e} \frac{j(j+1) + S(S+1) - N(N+1)}{2j(j+1)}\,, \tag{5}$$

where g_e is the Landé g value for the electron. Note that the quantum numbers are those of the radical in its excited electronic state, *i.e.* we have dropped the primes on the quantum numbers in this section.

In the case of orientation measurements[5], the term in the beat frequency, α_F, is reduced by a factor of 2. Furthermore, it is the normalized difference between the signals obtained using left and right circularly polarized light (I_L and I_R, respectively) that is fit with the expression

$$C = \frac{I_L - I_R}{I_L + I_R} = \mathrm{e}^{-k_\mathrm{d}t} \sum_F C'_F \cos\left(2\pi\alpha'_F H t + \phi\right) \tag{6}$$

with $\alpha'_F = \alpha_F/2$ to obtain the rate coefficients for collisional loss of orientation. A small contribution from the alignment in the denominator of this expression for the orientation signal could not be observed experimentally, and was neglected in the analysis[7].

Two phenomenological first order rate coefficients, k_p and k_d, have been introduced in Eq. (2) to allow for decay of population and angular momentum polarization, respectively[50,51]. The rate coefficients are dependent on the concentration of the collider, and can both be expressed as sums of rate coefficients describing collision-free and collisional-induced decay

processes

$$k_{\rm p} = k_0 + k_1\,[{\rm Ar}]$$
$$k_{\rm d} = k_2 + k_3\,[{\rm Ar}]\ . \qquad (7)$$

Note that in the present work, in which we do not resolve elastic depolarization[7], the population decay, characterized by $k_{\rm p}$, is associated with processes that remove OH(A), such as fluorescence (k_0) or electronic quenching (k_1), and not with processes such as RET that occur *within* the OH(A) electronic state[1,4]. k_2 is associated with depolarization in the absence of collisions with argon, which could arise, for example, from field inhomogeneities. Of particular interest to the current work is k_3, which accounts for the collisional depolarization of OH(A). This experimentally determined depolarization rate coefficient potentially contains an unwanted contribution due to dephasing of the quantum beat, and so can overestimate the value of the true depolarization rate coefficients[4]. However, as we will see in Section III C, simulations suggest that the dephasing effect is of very minor importance in the experiments presented below, and the experimentally determined rate coefficients, $k_3^{(k)}$, and cross sections, $\sigma_3^{(k)}$ (for specific polarization moments, k) are essentially equal to the collisional depolarization rates and cross sections, $k^{(k)}$, and cross sections, $\sigma^{(k)}$, of interest.

Typical OH(A) Zeeman quantum beat signals, obtained at a range of argon pressures, are shown in Fig. 1. We have demonstrated previously that the beat amplitudes are well-described by LIF linestrength theory[4,6]. For each rovibronic transition, a series of between 6 and 8 fluorescence decay curves obtained as a function of collider concentration were fitted globally, using the signal amplitudes, A, the relative beat amplitudes, C_F, the magnetic field H, the phase ϕ, and the four rate coefficients as adjustable parameters. The collisional quenching rate coefficients for OH(A) with Ar, which contribute to k_1, are relatively small and could be safely neglected in the analysis, although they were fixed to literature values[52,53]. Otherwise all the remaining parameters were optimized in the fits. Full details of the procedures employed have been given in previous publications[1,4–7]. As noted in the preceding subsection, to minimize the effects of translational moderation, for the experiments conducted under superthermal conditions, only the first 500 ns of the decay were analyzed, and the maximum pressure employed was around 400 mTorr. Errors were estimated using a Monte Carlo error routine described elsewhere[54].

III. DEPOLARIZATION CROSS SECTIONS: RESULTS AND DISCUSSION

In this section we will present new experimental thermally averaged (300 K) cross sections for the collisional loss of rotational angular momentum orientation (labelled forthwith collisional 'disorientation'), and new experimental cross sections for disorientation and the collisional loss of rotational alignment (labelled 'disalignment') under superthermal conditions. These will be compared with previously published thermally averaged (300 K) cross sections for disalignment of OH(A) by Ar[4]. We start, however, by presenting theoretical QM and QCT depolarization cross sections for the OH(A) + Ar system.

A. QM and QCT calculations under thermal and superthermal conditions

A full comparison of closed shell and open shell QM and QCT RET and collisional depolarization cross sections at fixed collision energies of 0.039 eV (left panels) and 0.40 eV (right panels) is shown in Fig. 2. The initial state is $N = 2$, and the cross sections are resolved in final rotational state, N'. A similar comparison of QM and QCT RET cross sections ($\sigma_{NN'}$) at a fixed collision energy 0.76 eV has also been performed, but for clarity is not presented in Fig. 2. The 'open shell' QCT values have been averaged over the two initially populated spin-rotation levels of the $N = 2$ rotational energy level of the radical and summed over the two spin-rotation states for each N'. Note that once averaged over initial and summed over final spin-rotation f_1 and f_2 levels, the open shell QM and QCT RET cross sections for each N' are indistinguishable from the closed shell QCT and QM results. The QM and QCT values are generally in excellent agreement, except for the RET cross sections when $N' = N \pm 1$. This is due to the binning procedure used in the QCT calculations, wherein trajectories with $|\Delta N| = |N' - N| > 0.5$ are considered inelastic[55], overestimating the cross section of the transitions into $N' = N \pm 1$. The rotational Gaussian binning procedure was also employed[56,57], which involves weighting more those trajectories with the correct rotational action, but the results were indistinguishable from those presented here using histogram binning (rounding to the nearest integer). Apart from this small discrepancy, the good level of agreement between the QCT and QM calculations justifies the use of the QCT results throughout most of the rest of the paper.

Raising the collision energy has rather a modest effect on the RET cross sections, although a wider range of final rotational states becomes accessible at higher energy. In Fig. 3 we plot the collision energy dependences of the total RET, disorientation and disalignment cross sections for OH(A) + Ar for the initial states $N = 2$ and $N = 14$. The range of collision energies covers both the thermal and superthermal measurements. For the RET cross sections, both QM and QCT data are present, and show excellent agreement across the entire range of collision energies presented. The panels showing the QCT disorientation and disalignment cross sections also include the QM data at 0.039 eV (for $N = 2$ and $N = 14$) and 0.40 eV (for $N = 2$) and show a similar excellent agreement with the QCT data. The RET inelastic scattering cross sections rise until the energies accessed are significantly in excess of rotational energy level spacing. Perhaps not surprisingly, while the total RET cross section for $N = 2$ is almost independent of $E_{\rm coll}$, that for $N = 14$ rises significantly until energies of around 1 eV are reached. By contrast, the depolarization cross sections, calculated using QCT methods, fall significantly with increasing energy around the very low collision energies sampled in the 300 K thermal experiments, but are then almost independent of energy for both OH(A) rotation rotational states studied. The contribution to the total depolarization cross sections from elastic collisions are also plotted in Fig. 3, and show a more monotonic decrease in magnitude with increasing collision energy. Notice that for sufficiently high initial N (N=14 for instance) elastic depolarization is the only contribution to the depolarization cross sections at low collision energies. The agreement with the QM data at 0.039 eV is also very good in this case, as can be seen in Fig. 3, and a similar degree of accordance can be expected at higher collision energies, similarly to the inelastic cross sections. The variations in cross section with collision energy suggest that OH(A) + Ar collisions leading to elastic and inelastic depolarization sample the attractive region of the potential more extensively than RET collisions. For high initial N, molecular rotation averages out the attractive potential making less effective not only the RET, but also the depolarization. Low energy collisions are highly depolarizing, but induce modest RET, whilst high energy collisions undergo more RET, but are significantly less depolarizing. Elastic depolarization becomes an increasingly minor process at high collision energies. The same general behavior as that shown in Fig. 3 is found for NO(A) + Ar, but in that system the smaller well-depth ensures that the cross sections vary significantly over a much reduced range of collision energies.

B. Thermal and superthermal depolarization cross sections: Experiment versus theory

The experimentally determined total depolarization cross sections for OH(A)+Ar as a function of the initial rotational state N are presented in Fig. 4. The left hand panels show the disorientation cross sections, $\sigma^{(1)}$, and the right hand panels the disalignment cross sections, $\sigma^{(2)}$, recorded under thermal ($\langle E_{\rm coll}\rangle = 0.039\,{\rm eV}$) and superthermal ($\langle E_{\rm coll}\rangle \approx 0.76\,{\rm eV}$ and $1.25\,{\rm eV}$) conditions. The full set of experimental and theoretical results are given in Tables I and II. The depolarization cross sections are found to decrease with increasing collision energy, consistent with the QCT data shown in Fig. 3. Given that the QCT calculations reveal that the RET cross sections increase as the collision energy is raised over the range probed experimentally here, as it becomes possible to populate more N' levels, and that the RET and depolarization cross sections are related by $\sigma_N^{(k)} = \sum_{N'} \sigma_{NN'}^{(k)}$, with $\sigma_{NN'}^{(k)}$ defined in Eq. (44) of the accompanying paper[20], it follows that the collisions become less depolarizing (*i.e.* $a^{(k)}(N, N')$ becomes more positive) as the collision energy increases. This corresponds to the collisions becoming more impulsive, a point that will be discussed in Section IV B. Other general features of the data shown in Fig. 4, such as the decrease in depolarization cross section with rotational quantum state, and smaller magnitude of the disorientation cross sections compared with those for disalignment have been discussed previously[4–7], and will not be commented on further here.

The experimental depolarization cross sections measured under thermal and superthermal conditions are also compared with theoretical QCT calculations in Fig. 4. The agreement between the experiment and theory is generally very good for the thermal disorientation and disalignment data (top two rows), and is qualitatively reasonable in the case of the superthermal data (bottom two rows). The QCT calculations shown in Fig. 3 reveal that the depolarization cross sections are very insensitive to collision energy at energies around those sampled in the superthermal experiments, and thus a precise modeling of the translational moderation is not required to obtain satisfactory agreement between experiment and theory. The experimental superthermal disorientation results are somewhat lower than the theoretical values, but given the uncertainties in the extent of translational moderation in these experiments, the main features of the experimental data are reproduced satisfactorily by theory. However, a number of simulations have been performed to check the validity of

the experimental data, and these are discussed briefly in the following sub-section.

C. Simulations of the experiment

Using the 'open shell' results from the QCT calculations it is possible to run detailed simulations of the experiment, as described fully elsewhere[4]. This allows the importance of dephasing, which is indistinguishable experimentally from collisional depolarization, to be determined. Dephasing occurs because each hyperfine and spin-rotation level of the radical has a different value of g_F. Therefore, when different hyperfine and spin-rotation levels are populated after the collision, the radical will precess at a slightly different frequency in the applied magnetic field. The total recorded signal is, therefore, a sum of many beat signals with slightly different frequencies, which leads to a loss of the beat even in the absence of collisional depolarization. The importance of dephasing depends on the extent to which collisions populate different final states, and on how depolarizing those collisions are. The effects of dephasing, as determined from the simulations[4], are shown in the upper four panels of Fig. 4. The difference between the QCT calculated depolarization cross sections and the simulation is very small. Dephasing makes a somewhat smaller contribution under thermal conditions than under superthermal conditions, because at the lower energy, the collisions are almost completely depolarizing, and therefore the states populated by collision are effectively unpolarized, and consequently have no dephasing effect on the polarization signal. Similar behaviour has also been observed previously in NO(A) + He and NO(A) + Ar[6]. Even under superthermal conditions, however, dephasing accounts for considerably less than 10 % of the cross section, showing that dephasing makes only a very minor contribution to the experimentally determined depolarization data presented here.

As noted above, significantly more RET occurs under superthermal conditions than at 300 K, especially for sufficiently high N states. The use of a monochromator to disperse the emission in the superthermal experiments means that fluorescence on emission branches at the edge of the monochromator bandwidth are less likely to be detected. This could lead to the observed experimental depolarization cross sections being smaller than the true values, and could explain some of the discrepancies between the experimental and theoretical superthermal disorientation cross sections. To ascertain the importance of this effect, further simulations were performed, in which emission from individual rotational states in OH(A)

was weighted by the appropriate monochromator transmission. However, the results from these weighted simulations, using realistic monochromator parameters, suggested the partial resolution of the emission had only a very minor effect on the returned experimental cross sections.

IV. MECHANISM: RESULTS AND DISCUSSION

Given the excellent agreement found between QM and QCT theory, and that the QCT calculations provide a satisfactory fit to the collisional depolarization data for both OH(A) + Ar and NO(A) + Ar[6], it seems reasonable to assume that the QCT calculations on the PESs employed will provide a realistic picture of the stereodynamics of these systems even at superthermal collision energies. At these collision energies one could expect some amount of vibrational excitation and thus a breakdown of the approximation based on keeping frozen the bond of the diatomic radical (NO or OH) at its equilibrium distance. Interestingly, however, disorientation and disalignment cross sections seem to be rather insensitive to the possible vibrational excitation and the approximation of a fixed internuclear distance seems to be adequate for the theoretical simulation of the experimental results. In this section we will compare the QCT results for OH(A) + Ar calculated at thermal (0.039 eV) and superthermal (0.76 eV) collision energies with those for NO(A) + Ar (0.039 eV). The main focus will be the comparison of the mechanism of collisional depolarization, and the effects that the PES, the radical mass combination, and the collision energy have on this. It should be noted that all the results presented in this section treat OH(A) and NO(A) as closed shell species, and therefore j and N can be used interchangeably.

A. Deflection functions (χ versus b)

The dependence of the deflection angle, χ (where the scattering and deflection angles are related by $\theta = |\chi|$), on the impact parameter, b, is presented in the top panels of Fig. 5 for OH(A) + Ar under thermal (left panel) and superthermal conditions (middle panel), and for NO(A) + Ar at 300 K (right panel). The figures group the trajectories into elastic (blue dots) and inelastic collisions (red dots), where the former includes all events for which $|\Delta N| \leq 0.5$. At very high impact parameters, all trajectories become elastic, as the collisions

become too 'glancing blow' to lead to inelastic scattering (or, indeed, elastic depolarization). However, it is also interesting to note that elastic scattering also takes place down to much smaller impact parameters, particularly in the case of OH(A) + Ar at 0.039 eV.

At lower impact parameters the collisions tend to probe the repulsive wall of the PES, and the deflection angles are seen to increase as the collisions become more 'head on'. These trajectories are classed as 'nearside', since the argon is scattered from the same side of the radical as that at which it approaches. As b increases, the Ar atom samples more attractive parts of the PES, which result in deflection angles in the range $-\pi \leq \chi \leq 0$ (or 'farside' scattering). The rainbow impact parameter can be easily identified for these collisions at $\approx$4 Å. Since the potential well in OH(A) + Ar is approximately a factor of 20 deeper than that in NO(A) + Ar, it leads to orbiting trajectories in which the Ar is trapped by the OH(A) and the H-atom is dragged around by the motion of the Ar. The complex can fall apart at any point during its rotation, leading to the curved structure observed in the top left panel of the figure. These orbiting trajectories also have positive time delays, as shown in the bottom left panel of the figure, corresponding to the Ar spending longer near the radical than it would in the absence of an interaction potential. The importance of these orbiting trajectories falls rapidly with increasing N, and for $N = 5$ at thermal collision energies orbiting trajectories play a relatively minor role. As the collision energy is increased, the time delay decreases, and the Ar is seen to travel too quickly to be able to fully sample the attractive part of the PES. The trends in the deflection function for OH(A) + Ar at these elevated collision energy collision conditions then resemble those for the much less attractive NO(A) + Ar system at low collision energies. The banded structures particularly visible in the plots for OH(A) + Ar at superthermal collision energies (middle panels) reflect scattering from either end of the OH(A) molecule. The structure becomes smeared-out at lower collision energies due to the influence of the attractive part of the potential, and are less clearly observable in the more symmetric NO(A) + Ar system.

B. Opacity functions

Fig. 6 compares the closed shell QM and QCT calculated opacity function for OH(A) + Ar and NO(A) + Ar. Apart from the rapid oscillatory structure in the OH(A) + Ar QM data arising from the deep potential energy well[2], there is excellent agreement once

more between the classical and quantum mechanical calculations. The QCT collisional depolarization moment-specific opacity functions, $P^{(k)}(b)$, are presented in Fig. 7. The probabilities of an elastic or inelastic collision (the latter summed over all final states); *i.e.* the opacity functions, $P^{(0)}(b)$, are shown as the dashed blue or red lines, respectively. Note that the $k = 0$ QCT opacity functions for elastic and inelastic collisions must sum to unity. Furthermore, the QCT elastic opacity functions, $P^{(0)}(b)$, tend to unity at large b because the QCT calculations are unable to converge the elastic cross sections. Elastic collisions are more prevalent in OH(A) + Ar than NO(A) + Ar at 0.039 eV. This reflects both the different locations of the center-of-mass in the two radicals, and the fact that the rotational energy level spacing in OH(A) is greater than in NO(A), and thus rotational energy transfer is less probable in the case of OH(A) than for NO(A). As N increases the proportion of inelastic collisions decreases as the rotational energy level spacing increases, to the point where there are no inelastic collisions for $N = 14$ in OH(A) + Ar at 0.039 eV. The range of impact parameters over which RET occurs is greater in NO(A) + Ar, reflecting the longer range of the NO(A)–Ar PES, and the relative ease with which rotational energy transfer occurs in this system. In addition, as can be seen in Fig. 6 and Fig. 7, the range of impact parameters leading to RET and to depolarization shrinks noticeably with increasing N, indicating that for high N values the contribution of the attractive part of the potential diminishes rapidly. This effect explains the lower values of the total cross section observed for high N states.

The continuous red and blue lines in the figures show the QCT disalignment opacity functions for inelastic and elastic collisions, $P^{(2)}(b)$, respectively. These have been calculated using the expression

$$P^{(k)}(b) = P^{(0)}(b)\left[1 - a^{(k)}(j)\right] \qquad \text{for} \quad k > 0\,, \tag{8}$$

where the depolarization parameters,

$$a^{(k)}(j) = \frac{\sum_{j'} \sigma_{j\to j'}\, a^{(k)}(j,j')}{\sigma_j}; \qquad \sigma_j = \sum_{j'} \sigma_{j\to j'} \tag{9}$$

have been averaged over final rotational state. Note that, unlike $P^{(0)}(b)$, these depolarization moment-specific opacity functions for $k > 0$ do not sum to unity over the elastic and inelastic trajectories. Furthermore, again unlike $P^{(0)}(b)$, it is possible to converge the elastic contributions to $P^{(k)}(b)$ for $k > 0$. The moment-specific opacity functions provide an indication of the extent to which the collisions cause angular momentum depolarization as a

function of the impact parameter. As a general trend, collisions lead to less depolarization as N increases. At higher N, the radical rotates faster, so that the Ar interacts with a more highly averaged, and hence more isotropic-looking potential. This averaging of the PES makes angular momentum transfer more difficult. For OH(A) + Ar at 0.039 eV, the collisions are completely depolarizing (*i.e.* $a^{(k)}(j) \sim 0$) over the range of b where RET occurs. The range of impact parameters at which elastic depolarization occurs is also greater than the range for RET, again reflecting the relative difficulty of inducing inelastic collisions in this system. This is particularly striking for the case of the $N = 5$ data for OH(A) + Ar, where elastic disalignment continues to contribute to relatively high impact parameters, where inelastic scattering plays no role, and where orbiting motion does not dominate (see the discussion in the preceding subsection). These high impact parameters correspond to the outer attractive rim of the potential, suggesting that at thermal collision energies OH(A) + Ar elastic collisional disalignment is strongly influenced by the long range potential, in contrast to what has been found here for NO(A) + Ar[6], and to some extent for OH(X) + Ar[16], for which the interaction potential is also much less attractive than for OH(A) + Ar. For NO(A) + Ar the range of RET and elastic depolarization is very similar: both elastic and inelastic collisions cause less depolarization than in OH(A) + Ar, reflecting the less attractive nature of the NO(A) + Ar interaction. Notice that the range of impact parameters at which both elastic and inelastic depolarization take place is significantly reduced for OH(A) + Ar at high N, consistent with the fact that the collisions become less influenced by the long range potential, and more impulsive in nature, as the initial rotational quantum state is increased (see Fig.7).

For OH(A) + Ar, collisions at the higher energy sample more the repulsive core of the PES, and the inelastic trajectories in particular become more impulsive and less depolarizing. Notice that the range of impact parameters at which elastic and inelastic depolarization take place is significantly reduced for OH(A) + Ar at the higher collision energy (see Fig.7). The opacity functions therefore start to resemble much more closely those shown for NO(A) + Ar at 0.039 eV. However, the range of impact parameters over which RET plays a role is smaller for superthermal OH(A) + Ar than for thermal NO(A) + Ar, resulting in smaller depolarization cross sections in the former case[6]. The differences in the opacity functions for OH(A) + Ar under thermal and superthermal conditions presented here also highlight the reasons, already discussed, for the trends in the experimental depolarization cross sections

with collision energy shown in Section III B.

C. Kinematics versus dynamics

The PESs clearly have a significant influence on the depolarization mechanisms for NO(A) + Ar and OH(A) + Ar. However, kinematics also plays an important role. To provide insight into the relative importance of kinematics, as opposed to the PES, trajectories were run for the initial state $N = 5$ using the OH mass combination on the NO(A)–Ar PES (denoted as ^{1}NO(A) + Ar) and for the NO masses on the OH(A)–Ar PES (denoted as O^{14}H(A) + Ar). The results from these calculations are presented in Fig. 8, along with those run for NO(A) + Ar (^{14}NO(A) + Ar) and OH(A) + Ar (O^{1}H(A) + Ar) on the correct PESs. The effect of changing the mass combination from that of OH(A) to NO(A) (*e.g.*, on going from ^{1}NO(A) + Ar to ^{14}NO(A) + Ar) is to increase the RET cross sections, and the number of N' levels populated after the collision. This is due to the different moments of inertia associated with the two mass combinations, which lead to a larger rotational energy level spacing for ^{1}NO than for ^{14}NO. For the same reason, elastic depolarization is significantly more important when the OH mass combination is used compared to that for NO. Changing the PES for the NO mass combination from that for ^{14}NO(A) + Ar to that for O^{14}H(A) + Ar results in a small decrease in the depolarization cross sections. This is mainly due to the decrease in the RET cross sections, since the depolarization moments do not change significantly, as is clear from the middle panels of the figure. This decrease in RET cross sections reflects the fact that the NO(A)–Ar PES is longer range than the OH(A)–Ar PES. However, changing the PES, but using the OH mass combination (*i.e.* going from ^{1}NO(A) + Ar to O^{1}H(A) + Ar) *increases* the RET cross sections. The NO(A)–Ar PES is insufficiently anisotropic to bring about significant RET when the energy level spacing of the radical is larger. Therefore, the values of the RET cross sections, and hence depolarization cross sections, are influenced both by the range and the anisotropy of the PES. Furthermore, both kinematic effects and the PES play significant roles in the collisional depolarization.

D. Vector correlations involving j'.

As discussed in detail in the accompanying paper[20], the kinematic apse for inelastic scattering is defined by the following equation[58]

$$\hat{\boldsymbol{a}} = \frac{\boldsymbol{k}' - \boldsymbol{k}}{|\boldsymbol{k}' - \boldsymbol{k}|} \,. \tag{10}$$

where $\boldsymbol{k}$ and $\boldsymbol{k'}$ are the initial and final relative velocities. It has been shown that purely impulsive collisions of rigid objects rigorously conserve the projection of $\boldsymbol{j}$ along the kinematic apse[59,60]. Fig. 9 presents histogram plots of the change in the projection of $\boldsymbol{j}$ onto the kinematic apse, $\Delta m_{\rm a} = m'_{\rm a} - m_{\rm a}$, where $m_{\rm a}$ and $m'_{\rm a}$ are the quantum numbers for the projections of $\boldsymbol{j}$ and $\boldsymbol{j}'$ onto $\boldsymbol{a}$, for the same data sets as shown in Fig. 7. Elastic depolarizing collisions are shown in blue whilst those for inelastic collisions are shown in red. Elastic depolarization is here defined as taking place if elastic trajectories, for which $|\Delta j| \leq 0.5$, give rise to a rotational angular momentum transfer quantum number, $K \geq 0.5$[3,20]. Such trajectories lead to a change in the direction of $\boldsymbol{j}$, but not its magnitude. Surprisingly, all of the cases presented in Fig. 9 show a strong propensity for conservation of the projection of $\boldsymbol{j}$ along the kinematic apse. As noted in the accompanying paper[20], this projection would be rigorously conserved in the limit of a purely impulsive collision, and as expected based on the foregoing discussion, NO(A) + Ar at 0.039 eV shows the strongest propensity for projection conservation of the three data sets presented. The conservation of the projection is also seen to improve with increasing N, and is more prevalent for elastic collisions than for inelastic collisions. In general, RET is likely to result in a more significant change in the direction of $\boldsymbol{j}$ than elastic depolarization and, therefore, the projection of $\boldsymbol{j}$ onto the apse is less likely to be conserved. As the collision energy is increased for OH(A) + Ar, the collisions tend to become less depolarizing and more impulsive. However, for inelastic scattering, the projection of $\boldsymbol{j}$ onto the apse is *less well* conserved at the higher collision energy. This is a somewhat surprising result, and suggests that simple arguments concerning the conservation of the projection of $\boldsymbol{j}$ along the kinematic apse should be treated with some caution. It probably arises because, although the collisions at high collision energy tend to be less depolarizing, more extensive RET takes place under these conditions, so that on average the projection along the kinematic apse is less well conserved.

To shed further light on the angular momentum depolarization in these systems, it is instructive to consider the triple vector correlations introduced in the accompanying paper[20].

To start with we present the $\boldsymbol{k}$-$\boldsymbol{k}'$-$\boldsymbol{j}'$ intrinsic portrait; *i.e.* the 3–D plot of the distribution of $\boldsymbol{j}'$ with respect to the $\boldsymbol{k}$-$\boldsymbol{k}'$ scattering plane. These are shown in Fig. 10 for OH(A) + Ar (left) and NO(A) + Ar (right) using the reference frame defined in Fig. 1a of the accompanying paper[20]. In these figures, the initial relative velocity vector, $\boldsymbol{k}$, defines the z-axis, and the x-axis points towards the bottom left of the figure. The zx-plane corresponds to the $\boldsymbol{k}$-$\boldsymbol{k}'$ scattering plane. The transition shown is $N = 2 \rightarrow N' = 3$ in both cases, and the $\boldsymbol{k}$-$\boldsymbol{k}'$-$\boldsymbol{j}'$ correlation has been integrated over $\boldsymbol{k}$-$\boldsymbol{k}'$ scattering angle, θ. Note that although the direction of $\boldsymbol{k}'$ is therefore not specified in these figures, the collision (scattering) plane still lies in the xz-plane. Both distributions are quite isotropic, although OH(A) + Ar is the more polarized of the two. Thus, while trajectories for OH(A) + Ar undergoing the $N = 2 \rightarrow N' = 3$ transition are slightly more coplanar than for NO(A) + Ar, neither system shows strong polarization with respect to the scattering plane.

Rather more revealing is the $\boldsymbol{k}$-$\boldsymbol{j}$-$\boldsymbol{j}'$ correlation 'portraits', which are presented in Fig. 11 for the same transition as in Fig. 10, using the reference frame defined in Fig. 1b of the accompanying paper[20], wherein the xz reference plane is defined by the $\boldsymbol{k}$ and $\boldsymbol{j}$ vectors. Again the x axis points towards the bottom left of the figures. The top panels of the figure correspond to when $\boldsymbol{k}$ and $\boldsymbol{j}$ are parallel (*i.e.* $\theta_j = 0°$), and the bottom panels to $\theta_j = 180°$. Note that the angles contribute roughly equally to the overall $\boldsymbol{k}$-$\boldsymbol{j}$-$\boldsymbol{j}'$ distribution, because the inelastic scattering channel in question shows no strong preference for where $\boldsymbol{j}$ lies in the reference frame shown. The $\boldsymbol{j}'$ distributions are seen to be significantly more polarized along the direction of $\boldsymbol{j}$ in NO(A) + Ar than in OH(A) + Ar. For NO(A) + Ar the direction of $\boldsymbol{j}$ is not altered significantly by the collision, whereas collisions in OH(A) + Ar are more depolarizing, and the distribution of $\boldsymbol{j}'$ is seen to be more isotropic with respect to $\boldsymbol{j}$.

By using the kinematic apse frame shown in Fig. 1c of the accompanying paper[20], it is possible to determine the $\boldsymbol{a}$-$\boldsymbol{j}$-$\boldsymbol{j}'$ correlation, and examples of this are shown in Fig. 12, again for the transition $N = 2 \rightarrow N' = 3$. In these figures, the kinematic apse, $\boldsymbol{a}$, lies along z, and the once again the x axis points towards the bottom left of the figures, with the xz plane containing the vectors $\boldsymbol{a}$ and $\boldsymbol{j}$. Analogous to Fig. 11, the correlation is shown at a range of angles between $\boldsymbol{a}$ and $\boldsymbol{j}$, $\theta_{aj} = 0°$ through to 180°. As with $\boldsymbol{k}$-$\boldsymbol{j}$-$\boldsymbol{j}'$ distribution, these angles contribute roughly equally to the overall $\boldsymbol{a}$-$\boldsymbol{j}$-$\boldsymbol{j}'$ distribution. Note that when $\theta_{aj} = 0°$, $\boldsymbol{j}$ lies along the apse, such that the xz-plane is undefined, and the distribution has cylindrical symmetry about the z-axis, a property also evident in the $\boldsymbol{k}$-$\boldsymbol{j}$-$\boldsymbol{j}'$ correlation plots of Fig.

11. Because the transition shown in the figure increases the magnitude of $\boldsymbol{j}$, in order for $\boldsymbol{j}'$ to have the same projection as $\boldsymbol{j}$ onto the kinematic apse, $\boldsymbol{j}'$ must lie in a cone around the z-axis. Therefore, this figure reinforces the results in Fig. 9, revealing that there is good conservation of the projection of $\boldsymbol{j}$ along the apse for both OH(A) + Ar (left panels) and NO(A) + Ar (right panels). Note that, broadly speaking, the behaviour of NO(A) + Ar is quite similar to that for NO(A) + He presented in the accompanying paper[20].

Although the projection of $\boldsymbol{j}$ along the apse is reasonably well conserved for both OH(A) and NO(A) + Ar, the plots in Fig. 12 reveal the $\boldsymbol{j}'$ distributions for OH(A) + Ar to be strikingly different to those for NO(A) + Ar in the apse frame. Whilst for the latter system, $\boldsymbol{j}'$ invariably lies in a small cone around the direction of $\boldsymbol{j}$, for OH(A) + Ar $\boldsymbol{j}'$ can also be found to lie in a narrow range at some other specific angles. For example, when $\boldsymbol{j}$ lies perpendicular to $\boldsymbol{a}$, $\boldsymbol{j}'$ is seen to point near equally either parallel or anti-parallel to $\boldsymbol{j}$ for OH(A) + Ar (bottom left panel), but almost exclusively parallel to $\boldsymbol{j}$ for NO(A) + Ar (bottom right panel). The behaviour for OH(A) is quite surprising, since it suggests that although the projection along the kinematic apse is conserved, it is nearly as equally likely for the OH(A) radical to finish rotating in the opposite sense, but in the same plane, as it was initially. This can be attributed to the attractive nature of the OH(A)–Ar PES, and to the fact that the H-atom is very light. As the Ar approaches, the attraction between the H and Ar can change the direction of the rotation of the radical. Note that, while the well-depth between the O end of the radical is greater than that with the H-end of the radical[2], the light mass of the H atom means that it is much more likely to swing around and meet the Ar before the latter can sample the potential well at the O-end of the OH(A) molecule. When $\boldsymbol{j}$ lies perpendicular to the apse, such that the forces act primarily in the plane of the diatomic, two classes of trajectories can be envisaged. In the first, the sense of rotation of the OH(A) is the same as the motion of the Ar, and the attraction of the passing Ar atom accelerates the rotation of the OH(A) from $N = 2$ to $N' = 3$. This would result in $\boldsymbol{j}'||\boldsymbol{j}$. In the second case, the OH(A) radical rotates so that the motion of the H-atom is in the opposite direction to that of the incoming Ar. Because the H-atom is so light, the attraction to the Ar atom is sufficiently strong to induce rotation of OH(A) in the opposite direction, leading to an anti-parallel orientation of $\boldsymbol{j}'$ with respect to $\boldsymbol{j}$, as shown in the middle left panel of Fig. 12. When $\boldsymbol{j}$ lies at an angle other than 90° to the apse (*e.g.*, at around 45°, as shown in the second row of Fig. 12), the forces do not act in the OH(A) rotation plane. The

strong attraction of the H-atom to the passing Ar atom can then cause a reorientation of the collision plane, which leads to the 'rabbit-ear' structure shown in the left-hand second panel of the figure. Again this structure is almost absent in the less attractive, and kinematically very different, NO(A) + Ar system (right-hand second panel).

The interesting structures shown in Fig. 12 for OH(A) + Ar are particularly revealing about the roles played in angular momentum depolarization by the PES and by the kinematics of the diatomic radical. Increasing the initial or final OH(A) rotational angular momentum, or increasing the collision energy, results in the plots of the $\boldsymbol{a}$-$\boldsymbol{j}$-$\boldsymbol{j}'$ distribution becoming more impulsive in nature, and more similar to those shown for NO(A) + Ar in the right panels of Fig. 12. In the latter system, the PES is insufficiently attractive to significantly perturb the motion of the radical as the Ar approaches, unless the collision is a direct impulsive encounter. Furthermore, the center-of-mass of NO(A) is located near the center of the bond, such that approach from either end of the molecule is equally favored. Therefore, in the case of NO(A) + Ar, the direction of $\boldsymbol{j}'$ in the kinematic apse frame is determined purely by the direction in which the impulse acts, leading to an oriented angular momentum distribution in the $\boldsymbol{k}$-$\boldsymbol{j}$-$\boldsymbol{j}'$ or $\boldsymbol{a}$-$\boldsymbol{j}$-$\boldsymbol{j}'$ frames.

V. CONCLUSIONS

Zeeman quantum beat spectroscopy has been used to study the collisional depolarization of OH(A) by Ar over a range of collision energies. New depolarization cross sections have been presented for collisional loss of rotational angular momentum orientation and alignment, and shown to decrease as the collision energy and initial rotation state N are raised. The experimental cross sections generally agree well with the results from QCT and QM calculations.

A collision energy dependent theoretical study of the mechanism of collisional depolarization has also been presented for OH(A) + Ar and NO(A) + Ar. Part of this work exploits the new theoretical framework for the study of $\boldsymbol{k}$-$\boldsymbol{j}$-$\boldsymbol{j}'$ vector correlations developed in the accompanying paper[20]. Impulsive encounters dominate in the case of NO(A) + Ar, resulting in depolarization being inefficient compared to RET, and a dominance of 'nearside' scattering. In contrast, orbiting trajectories are observed in OH(A) + Ar at thermal collision energies, and the highly attractive and anisotropic nature of the PES effectively leads to

randomization of the direction of $\boldsymbol{j}$ after every collision. However, even for OH(A) + Ar at close to thermal 300 K collision energies, there is a strong propensity for the projection of $\boldsymbol{j}$ onto the kinematic apse to be conserved. As the collision energy is increased, the collisions start to probe the repulsive wall of the OH(A)–Ar PES, as opposed to the long range attractive region, and the dynamics begins to resemble more that observed in NO(A) + Ar.

Acknowledgments

The support of the UK EPSRC (to M.B. *via* Programme Grant No. EP/G00224X/1), the EU (to M.B. *via* FP7 EU People ITN project 238671), and the Spanish Ministry of Science and Innovation (grants CTQ2008-02578/BQU and Consolider Ingenio 2010 CSD2009-00038) are gratefully acknowledged. J.K. acknowledges financial support from the US National Science Foundation (grant No. CHE-0848110 to Professor M.H. Alexander) and the University Complutense de Madrid/Grupo Santander (under the "Movilidad de Investigadores Extranjeros" programme). Finally, we thank Professor K.G. McKendrick and Dr M.L. Costen for valuable discussions, and Richard Muckle and Alexander Bryant for help with obtaining some of the data presented in this paper.

REFERENCES

[1]M. Brouard, A. Bryant, I. Burak, F. Quadrini, S. Marinakis, I. A. Garcia, and C. Vallance, Mol. Phys. **103**, 1693 (2005).

[2]J. Kłos, M. H. Alexander, M. Brouard, C. J. Eyles, and F. J. Aoiz, J. Chem. Phys. **129**, 054301 (2008).

[3]F. J. Aoiz, M. Brouard, C. J. Eyles, J. Kłos, and M. P. de Miranda, J. Chem. Phys. **130**, 044305 (2009).

[4]M. Brouard, A. Bryant, Y.-P. Chang, R. Cireasa, C. J. Eyles, A. M. Green, S. Marinakis, F. J. Aoiz, and J. Kłos, J. Chem. Phys. **130**, 044306 (2009).

[5]M. Brouard, H. Chadwick, Y.-P. Chang, R. Cireasa, and C. J. Eyles, Physica Scripta **80**, 048120 (2009).

[6]M. Brouard, H. Chadwick, Y.-P. Chang, R. Cireasa, C. J. Eyles, A. O. L. Via, N. Screen, F. J. Aoiz, and J. Kłos, J. Chem. Phys. **131**, 104307 (2009).

[7]M. L. Costen, R. Livingstone, K. G. McKendrick, G. Paterson, M. Brouard, H. Chadwick, Y.-P. Chang, C. J. Eyles, F. J. Aoiz, and J. Kłos, J. Phys. Chem. A **113**, 15156 (2009).

[8]H. J. Crichton, M. L. Costen, and K. G. McKendrick, J. Chem. Phys. **119**, 9461 (2003).

[9]M. L. Costen, H. J. Crichton, and K. G. McKendrick, J. Chem. Phys. **120**, 7910 (2004).

[10]S. Marinakis, G. Paterson, J. Kłos, M. L. Costen, and K. G. McKendrick, Phys. Chem. Chem. Phys. **9**, 4414 (2007).

[11]S. Marinakis, G. Paterson, G. Richmond, M. Rockingham, M. L. Costen, and K. G. McKendrick, J. Chem. Phys. **128**, 021101 (2008).

[12]G. Paterson, S. Marinakis, M. L. Costen, K. G. McKendrick, J. Kłos, and R. Tobota, J. Chem. Phys. **129**, 074304 (2008).

[13]G. Paterson, S. Marinakis, J. Kłos, M. L. Costen, and K. G. McKendrick, Phys. Chem. Chem. Phys. **11**, 8804 (2009).

[14]G. Paterson, S. Marinakis, M. L. Costen, and K. G. McKendrick, Phys. Chem. Chem. Phys. **11**, 8813 (2009).

[15]I. Ballingall, M. Rutherford, K. McKendrick, and M. Costen, Mol. Phys. **108**, 847 (2010).

[16]P. J. Dagdigian and M. H. Alexander, J. Chem. Phys. **130**, 094303 (2009).

[17]P. J. Dagdigian and M. H. Alexander, J. Chem. Phys. **130**, 164315 (2009).

[18]P. J. Dagdigian and M. H. Alexander, J. Chem. Phys. **130**, 204304 (2009).

[19]L. Ma, M. H. Alexander, and P. J. Dagdigian, J. Chem. Phys. **134**, 154307 (2011).

[20]M. Brouard, H. Chadwick, C. J. Eyles, F. J. Aoiz, and J. Kłos, J. Chem. Phys. (2011).

[21]J. Kłos, M. H. Alexander, R. Hernández-Lamoneda, and T. G. Wright, J. Chem. Phys. **129**, 244303 (2008).

[22]F. J. Aoiz, L. Bañares, T. Díez-Rojo, V. J. Herrero, and V. S. Rábanos, J. Phys. Chem. **100**, 4071 (1996).

[23]F. J. Aoiz, L. Bañares, and V. J. Herrero, J. Chem. Soc., Faraday Trans. **94**, 2483 (1998).

[24]HIBRIDON is a package of programs for the time-independent quantum treatment of inelastic collisions and photodissociation written by M. H. Alexander, D. Manolopoulos, H.-J. Werner, and B. Follmeg, with contributions by P. F. Vohralik, D. Lemoine, G. Corey, R. Gordon, B. Johnson, T. Orlikowski, A. Berning, A. Degli-Esposti, C. Rist, P. Dagdigian, B. Pouilly, G. van der Sanden, M. Yang, F. de Weerd, S. Gregurick, and J. Klos.

[25]D. E. Manolopoulos, J. Chem. Phys. **85**, 6425 (1986).

[26]M. H. Alexander and D. E. Manolopoulos, J. Chem. Phys. **86**, 2044 (1987).

[27]K. H. Gericke, S. Klee, F. J. Comes, and R. N. Dixon, J. Chem. Phys. **85**, 4463 (1986).

[28]A. U. Grunewald, K. H. Gericke, and F. J. Comes, J. Chem. Phys. **87**, 5709 (1987).

[29]A. U. Grunewald, K. H. Gericke, and F. J. Comes, J. Chem. Phys. **89**, 345 (1988).

[30]R. N. Dixon, J. Nightingale, C. M. Western, and X. Yang, Chem. Phys. Lett. **151**, 328 (1988).

[31]K. H. Gericke, H. G. Gläser, C. Maul, and F. J. Comes, J. Chem. Phys. **92**, 411 (1990).

[32]M. P. Docker, A. Hodgson, and J. P. Simons, Faraday Discuss. Chem. Soc. **82**, 25 (1986).

[33]J. August, M. Brouard, M. P. Docker, A. Hodgson, C. J. Milne, and J. P. Simons, Ber. Bunsenges. Phys. Chem. **92**, 264 (1988).

[34]M. Brouard, M. T. Martinez, C. J. Milne, and J. P. Simons, Chem. Phys. Lett. **165**, 423 (1990).

[35]A. J. Alexander, Phys. Rev. A **66**, 060702 (2002).

[36]A. J. Alexander, J. Chem. Phys. **118**, 6234 (2003).

[37]"*LIFBASE: Database and simulation program (v. 1.6).*" J. Luque and D. R. Crosley, SRI International Report MP 99-009, (1999).

[38]P. Lebow, F. Raab, and H. Metcalf, Phys. Rev. Lett. **42**, 85 (1979).

[39]F. Raab, T. Bergeman, D. Lieberman, and H. Metcalf, Optics Lett. **5**, 427 (1980).

[40]F. Raab, T. Bergeman, D. Lieberman, and H. Metcalf, Phys. Rev. A **24**, 3120 (1981).

[41]R. T. Carter, I. M. Povey, H. Bitto, and J. R. Huber, J. Chem. Phys. **104**, 5365 (1996).

[42]J. Xin and S. A. Reid, J. Chem. Phys. **112**, 10067 (2000).

[43]J. Xin and S. A. Reid, J. Chem. Phys. **116**, 525 (2002).

[44]J. Xin, I. Ionescu, D. Kuffel, and S. A. Reid, Chem. Phys. **291**, 61 (2003).

[45]A. U. Grunewald, K. H. Gericke, and F. J. Comes, Chem. Phys. Lett. **132**, 121 (1986).

[46]M. Baba, M. Brouard, S. P. Rayner, and J. P. Simons, Chem. Phys. Lett. **220**, 411 (1994).

[47]J. J. ter Meulen, W. A. Majewski, W. L. Meerts, and A. Dymanus, Chem. Phys. Lett. **94**, 25 (1983).

[48]J. J. ter Meulen, W. Ubachs, and A. Dymanus, Chem. Phys. Lett. **129**, 533 (1986).

[49]Y.-P. Chang, M. Brouard, R. Cireasa, T. Perkins, and S. A. Seamons, Phys. Chem. Chem. Phys. **13**, 8213 (2011).

[50]P. J. Brucat and R. N. Zare, J. Chem. Phys. **78**, 100 (1983).

[51]P. J. Brucat and R. N. Zare, J. Chem. Phys. **81**, 2562 (1984).

[52]P. H. Paul, J. Quant. Spec. Radiat. Transf. **51**, 511 (1994).

[53]K. H. Becker, D. Haaks, and T. Tatarczyk, Chem. Phys. Lett. **25**, 564 (1974).

[54]M. Brouard, I. Burak, S. D. Gatenby, D. Hart, and D. Minayev, J. Chem. Phys. **110**, 11335 (1999).

[55]F. J. Aoiz, J. E. Verdasco, V. J. Herrero, V. S. Rábanos, and M. H. Alexander, J. Chem. Phys. **119**, 5860 (2003).

[56]L. Bañares, F. J. Aoiz, P. Honvault, B. Bussery-Honvault, and J. M. Launay, J. Chem. Phys. **118**, 565 (2003).

[57]L. Bonnet and J.-C. Rayez, Chem. Phys. Lett. **397**, 106 (2004).

[58]A. J. McCaffery, M. J. Proctor, and B. J. Whitaker, Annu. Rev. Phys. Chem. **37**, 223 (1986).

[59]V. Khare, D. J. Kouri, and D. K. Hoffman, J. Chem. Phys. **74**, 2275 (1981).

[60]D. K. Hoffman, J. W. Evans, and D. J. Kouri, J. Chem. Phys. **80**, 144 (1984).

[61]The data for $N = 2$ collisional disalignment recorded under thermal conditions reported previously[4] were obtained with a mis-calibrated pressure gauge, and these experimental results have been corrected in the present work. The remaining values are a reanalysis of the original data set have changed very slightly from those published. It should also be noted that the QCT elastic depolarization cross sections reported in that work for $N = 8$ and $N = 14$ were slightly underestimated due to use of a $b_{\max}$ value which was too small. This has also been corrected in the present work. One of the conclusions of our previous paper[4] was that the QCT collisional disalignment cross sections were around ten percent smaller than the experimental ones for the initial f_1 spin-rotation states. Whilst this remains largely true in the present revised data set for these levels, it should be noted that the new disorientation and disalignment data presented here for the f_2 state under thermal conditions, and for both the f_1 and f_2 states under superthermal conditions, does not show a clear systematic disagreement with theory. The same conclusion was also drawn for the elastic depolarization measurements reported recently by McKendrick, Costen, and Brouard and coworkers[7].

		$N=0$	$N=1$		$N=2$		$N=5$		$N=8$		$N=14$	
		f_1	f_1	f_2	f_1	f_2	f_1	f_2	f_1	f_2	f_1	f_2
Thermal	Experiment	34(14)	40(15)	—	—	51(17)	—	41(9)	—	32(11)	21(5)	15(7)
(300 K)	QCT total	24.6	36.1	66.3	34.1	52.8	30.1	37.8	21.5	25.3	10.3	11.5
	QCT elastic	0.0	9.6	16.4	9.4	14.7	11.3	14.2	14.1	16.9	8.6	9.8
	QCT SR changing	—	10.7	21.5	8.7	13.1	8.4	10.1	6.6	7.5	1.7	1.8
Superthermal	Experiment	—	—	—	—	15(8)	—	15(6)	—	11(5)	—	11(3)
(248 nm)	QCT total	34.5	29.6	43.1	24.3	33.3	19.2	23.1	14.7	16.9	7.8	8.5
	QCT elastic	0.0	2.2	4.2	2.1	3.0	1.6	1.9	1.5	1.8	1.7	1.9
	QCT SR changing	—	2.3	4.5	2.2	3.4	1.5	1.8	0.8	1.0	0.5	0.6
Superthermal	Experiment	—	—	—	—	22(7)	—	22(4)	—	13(3)	9(2)	—
(193 nm)	QCT total	33.7	29.9	41.2	26.6	34.1	20.8	24.7	15.2	17.5	7.7	8.5
	QCT elastic	0.0	1.6	3.2	1.6	2.3	1.3	1.5	1.1	1.3	1.2	1.3
	QCT SR changing	—	1.6	3.2	1.7	2.6	1.5	1.8	0.8	0.9	0.4	0.4

TABLE I. Cross sections for collisional disorientation ($\sigma^{(1)}/\text{Å}^2$) of OH(A) by Ar under thermal and superthermal conditions. The QCT calculations were performed at collision energies 0.039 eV (labelled thermal 300 K), 0.76 eV (superthermal, 248 nm photolysis) and 1.25 eV (superthermal, 193 nm photolysis). The error bars (indicated in brackets on the experimental data) were determined using a Monte Carlo procedure[54], and represent 95 % confidence limits. 'SR changing' refers to 'pure' spin-rotation changing collisions, for which $\Delta N = 0$, but $\Delta j = \pm 1$.

		$N=1$	$N=2$		$N=5$		$N=8$		$N=14$	
		f_1	f_1	f_2	f_1	f_2	f_1	f_2	f_1	f_2
Thermal*	Experiment	58(13)	59(14)	66(15)	71(12)	64(14)	51(14)	—	23(5)	—
(300 K)	QCT total	59.8	55.5	67.0	50.6	57.0	45.6	50.4	26.2	28.9
	QCT elastic	23.3	21.4	25.1	24.3	26.7	31.6	34.7	22.2	24.6
	QCT SR changing	10.0	9.8	14.7	11.4	13.7	12.5	14.0	4.0	4.3
Superthermal	Experiment	—	—	29(11)	—	30(3)	—	22(5)	—	17(6)
(248 nm)	QCT total	40.9	33.4	39.2	26.0	28.8	21.2	23.1	13.9	15.1
	QCT elastic	5.4	4.6	5.5	3.4	4.0	3.6	4.2	4.4	4.9
	QCT SR changing	2.2	2.1	3.2	1.3	1.6	0.9	1.0	0.7	0.8
Superthermal	Experiment	—	—	27(8)	27(9)	25(6)	—	21(6)	19(5)	19(6)
(193 nm)	QCT total	39.3	33.8	38.6	26.3	28.1	20.9	22.4	13.1	14.2
	QCT elastic	4.0	3.6	4.2	2.6	2.8	2.5	2.9	3.0	3.4
	QCT SR changing	1.6	1.6	2.5	1.3	1.5	0.8	0.9	0.5	0.5

TABLE II. As for Table I, but showing the cross sections for collisional 'disalignment' ($\sigma^{(2)}/\text{Å}^2$) of OH(A) by Ar under thermal and superthermal conditions. *Note that some of the collisional disalignment data obtained under thermal conditions presented here are a reanalysis of that shown previously in ref. 4. See ref. 61.

FIG. 1. Color online: Typical orientation Zeeman quantum beat data recorded at a range of Ar pressures following OH(A) excitation on the $R_{11}(13)$ transition (dashed black line), and a fit to the data (solid red line) following the procedures discussed in the text. The signal was obtained using the photodissociation of H_2O_2 at a wavelength of 193 nm as the source of OH, and using a magnetic field of approximately 25 Gauss.

FIG. 2. Color online: Comparison of the theoretical RET cross sections, and collisional 'disorientation' and 'disalignment' cross sections for $N = 2$ resolved in N', calculated using closed shell QCT (filled circles), closed shell QM (filled squares), 'open shell' QCT (open triangles), and 'open shell' QM (open squares)for OH(A) + Ar at fixed collision energies of 0.039 eV (left panels) and superthermal, fixed collision energy 0.40 eV (right panels). The 'open shell' QCT and QM results have been averaged over the initially populated spin-rotation levels and summed over final.

FIG. 3. Color online: Closed shell QM (points) and QCT (continuous lines) calculated excitation functions OH(A) + Ar for initial states $N = 2$ and $N = 14$, summed over all final states where appropriate. RET cross sections are shown in red in the top panels, while total disorientation and disalignment cross sections are shown in the middle and bottom panels, respectively. Also shown as the dashed lines in the lower four panels are the contributions from elastic collisions to the total depolarization cross sections. The QM data for the collisional depolarization cross sections were obtained at 0.039 eV and 0.40 eV for $N = 2$ and 0.039 eV for $N = 14$.

FIG. 4. Color online: Comparison of the experimental total depolarization cross sections (filled black triangles for f_1 states, circles for f_2 states) for OH(A) + Ar versus initial rotational state with the 'open shell' QCT calculations (open blue triangles, f_1, and circles,f_2) and simulations (filled red squares) for disorientation (left panels) and disalignment (right panels) under thermal conditions (top two rows), and superthermal conditions, following the photodissociation of H_2O_2 at 248 nm (third row) and at 193 nm (bottom row). The experimental error bars represent 95 % confidence limits[54]. Some of the collisional disalignment data obtained under thermal conditions presented here are the result of a reanalysis of those data shown previously in ref. 4 (see ref. 61). The 300 K thermal data employed a mean relative velocity of 730 m s^{-1}, while the superthermal data assumed velocities of 3900 m s^{-1} and 3300 m s^{-1} for photolysis at 193 nm and 248 nm, respectively, with the exception of the $N = 14$ data at 248 nm, which employed 2800 m s^{-1}.

FIG. 5. Color online: Top panels: Scatter plots of deflection angle, χ, versus impact parameter, b, for OH(A) + Ar at a fixed collision energy of 0.039 eV (left panels) and under superthermal conditions (middle panels), and for NO(A) + Ar at 0.039 eV (right panels) showing the nearside-farside scattering nature of the trajectories. Bottom panels: The time delay associated with b for the same systems. Elastic trajectories, for which $|\Delta N| \leq 0.5$, are shown in blue and inelastic in red.

FIG. 6. Color online: Comparison of the closed shell QM (continuous black lines) and QCT (dashed red lines) total (summed over final states with $|\Delta N| > 0.5$) opacity functions for inelastic collisions of OH(A) + Ar under thermal, 0.039 eV (left panels) and superthermal, 0.76 eV (middle panels) conditions and for NO(A) + Ar (right panels). The top panels are $N = 2$, the middle panels $N = 5$, and bottom panels $N = 14$. It should be noted that there are no inelastic collisions for $N = 14$ in OH(A) + Ar under thermal conditions.

FIG. 7. Color online: Closed shell QCT opacity functions for elastic (bold blue dashes) and inelastic (red dashes) collisions for OH(A) + Ar under thermal (left panels) and superthermal (middle panels) conditions and for NO(A) + Ar (right panels). The solid lines correspond to the disalignment opacity functions for the same conditions. The top panels are for the $N = 2$ initial state, the middle panels for $N = 5$, and bottom panels for $N = 14$. It should be noted that there are no inelastic collisions for $N = 14$ in OH(A) + Ar under thermal conditions. In this figure elastic trajectories include all trajectories for which $|\Delta N| \leq 0.5$.

FIG. 8. Color online: Comparison of the thermal (fixed $E_{\rm coll}$=0.039 eV) QCT RET N' state resolved integral cross sections (top panel), depolarization moments (middle panels), and depolarization cross sections (bottom panels) from $N = 5$, illustrating the effects of the PES versus kinematics (see text for details).

FIG. 9. Color online: Histogram plots of the change in the projection of $\boldsymbol{j}$ onto the kinematic apse, $\boldsymbol{a}$, $\Delta m_a = m'_a - m_a$, due to collisions for thermal OH(A) + Ar (left panels), superthermal OH(A) + Ar (middle panels), and thermal NO(A) + Ar (right panels). The top panels are for initial $N = 2$, the middle for $N = 5$ and the bottom $N = 14$. Elastic depolarizing trajectories are shown in blue and inelastic in red. Notice that this set of elastic trajectories include those for which $|\Delta N| \leq 0.5$, but, additionally, for which the rotational angular momentum transfer quantum number $K \geq 0.5$, thus implying a change in the direction of N. Note that there are no inelastic collisions for $N = 14$ in OH(A) + Ar under thermal conditions.

FIG. 10. Color online: The $\boldsymbol{k}$-$\boldsymbol{k}'$-$\boldsymbol{j}'$ distribution for OH(A) + Ar (left) and NO(A) + Ar (right) at a collision energy of 0.039 eV for $N = 2 \rightarrow N' = 3$. The distributions are averaged over scattering angle ($\cos\theta = \hat{\boldsymbol{k}} \cdot \hat{\boldsymbol{k}}'$).

FIG. 11. Color online: The $\boldsymbol{k}$-$\boldsymbol{j}$-$\boldsymbol{j}'$ distribution for $N = 2 \rightarrow N' = 3$. The left hand panels are OH(A) + Ar and the right hand panels NO(A) + Ar at 300 K. The top row corresponds to $\theta_j = 0°$, and the bottom to $\theta_j = 180°$, with a selection of angles in between. The red vector indicates the direction of $\boldsymbol{j}$, which lies in the xz plane, $z \equiv \hat{\boldsymbol{k}}$.

FIG. 12. Color online: As for figure 11, but showing the $\boldsymbol{a}$-$\boldsymbol{j}$-$\boldsymbol{j}'$ distribution for $N = 2 \rightarrow N' = 3$. The left hand panels are OH(A) + Ar and the right hand panels NO(A) + Ar at 300 K. The top row corresponds to $\theta_{aj} = 0°$ and the bottom to $\theta_{aj} = 180°$, with selected angles in between.

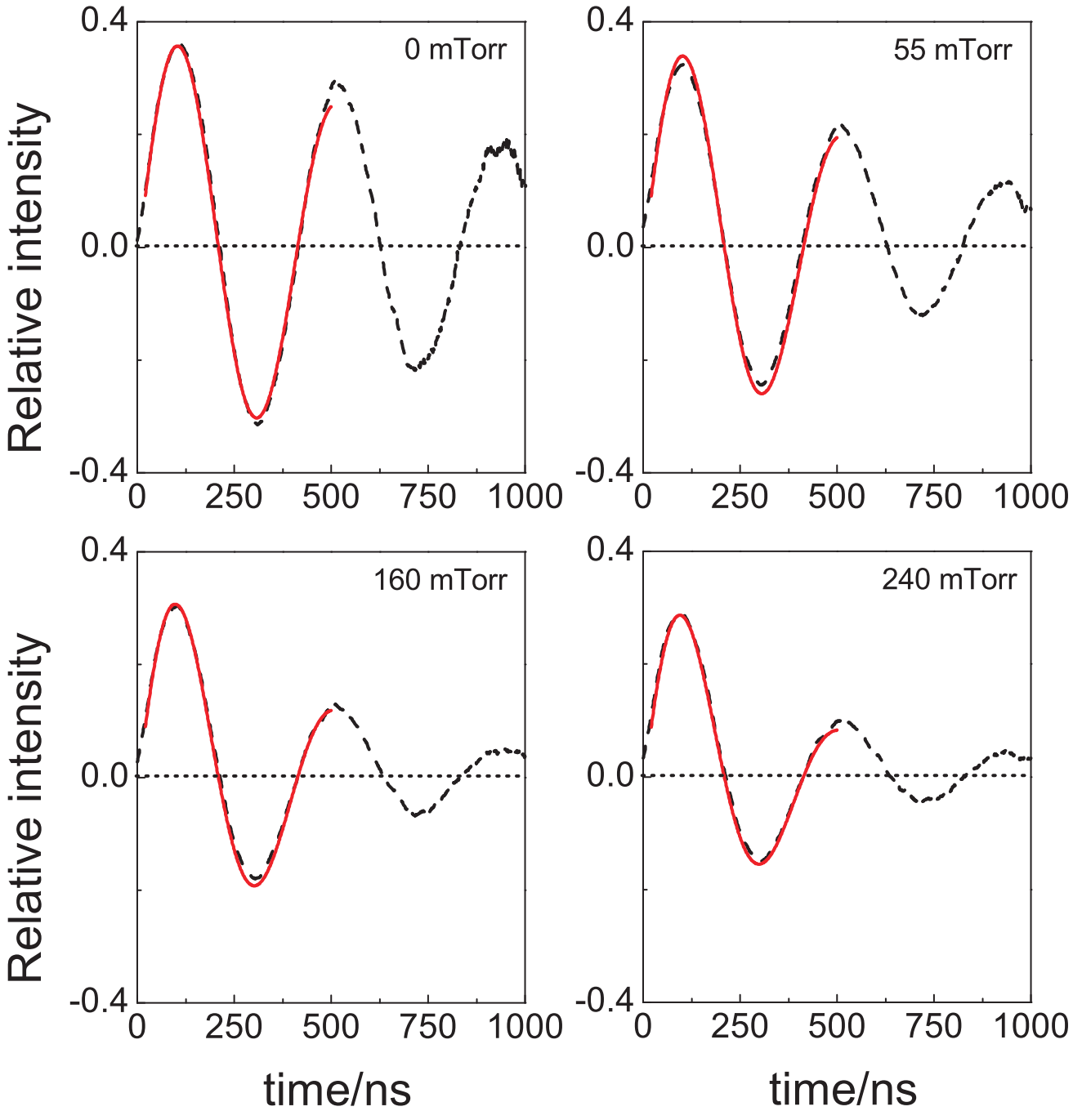
0 mTorr
55 mTorr
160 mTorr
240 mTorr
Relative intensity
Relative intensity
time/ns
time/ns
0.4
0.0
-0.4
0
250
500
750
1000

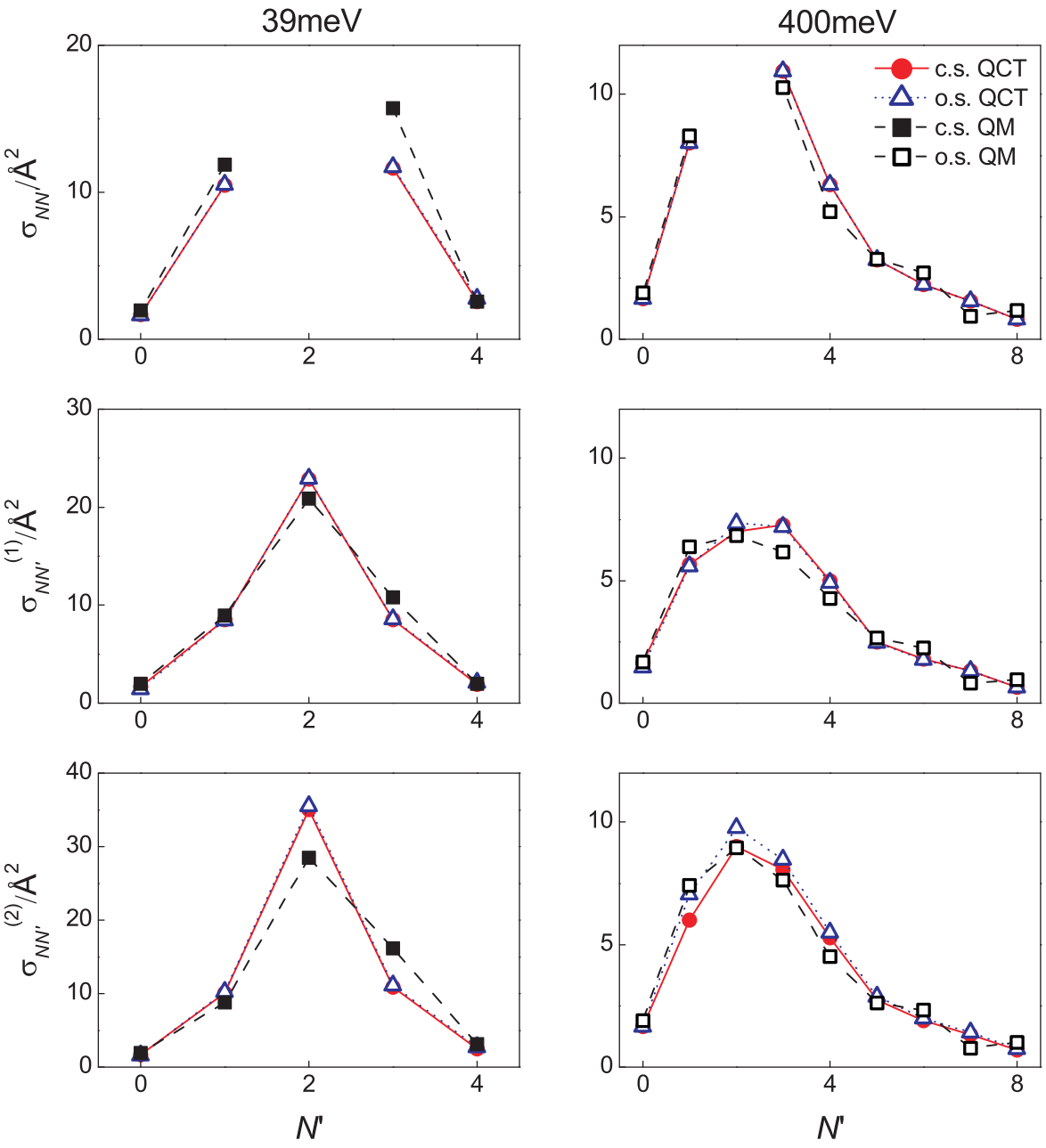
39meV
400meV
c.s. QCT
o.s. QCT
c.s. QM
o.s. QM
σ_NN'/Å^2
σ_NN'^(1)/Å^2
σ_NN'^(2)/Å^2
N'
N'

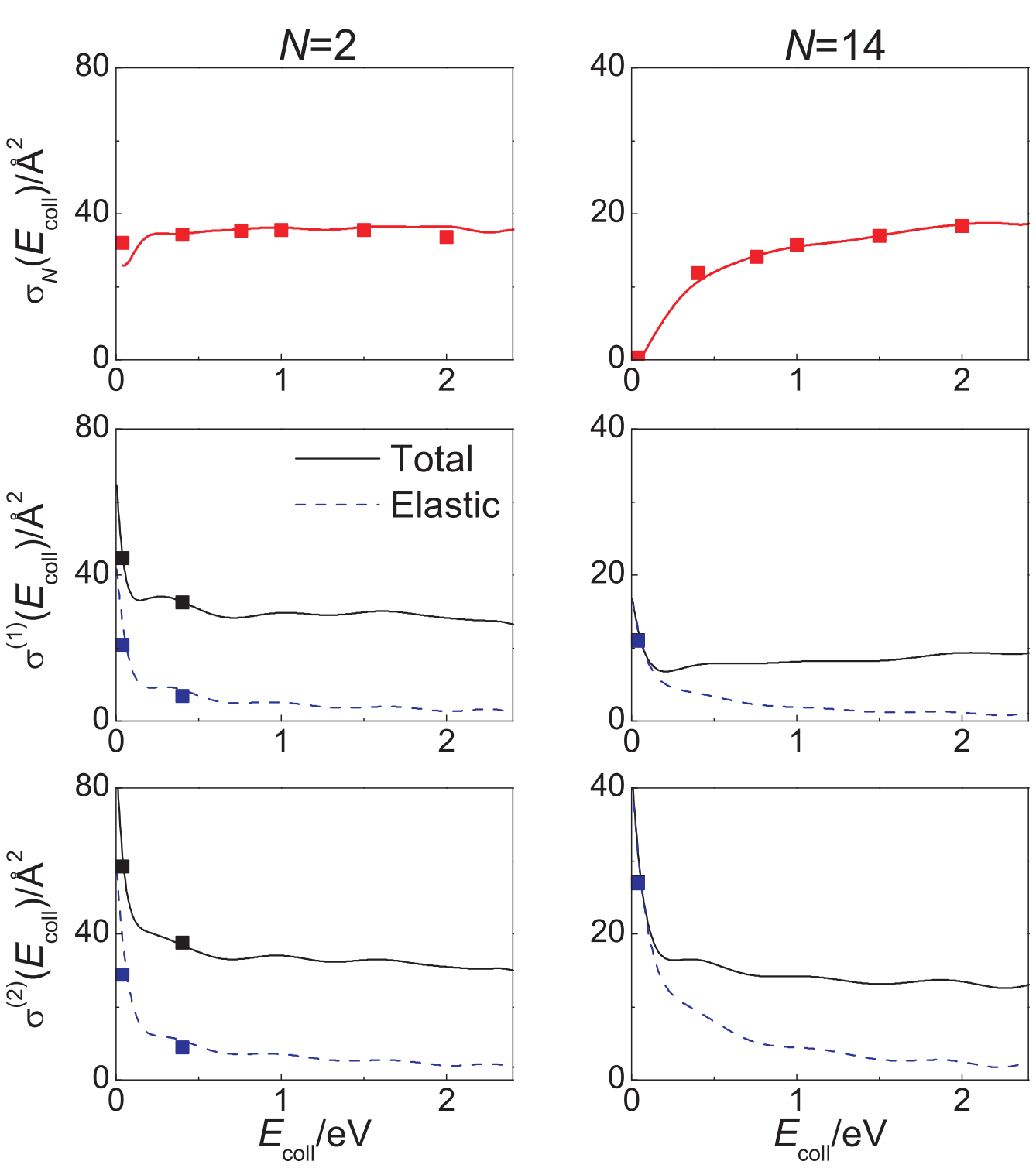
N=2
N=14
Total
Elastic
σN(Ecoll)/Å2
σ(1)(Ecoll)/Å2
σ(2)(Ecoll)/Å2
Ecoll/eV
Ecoll/eV

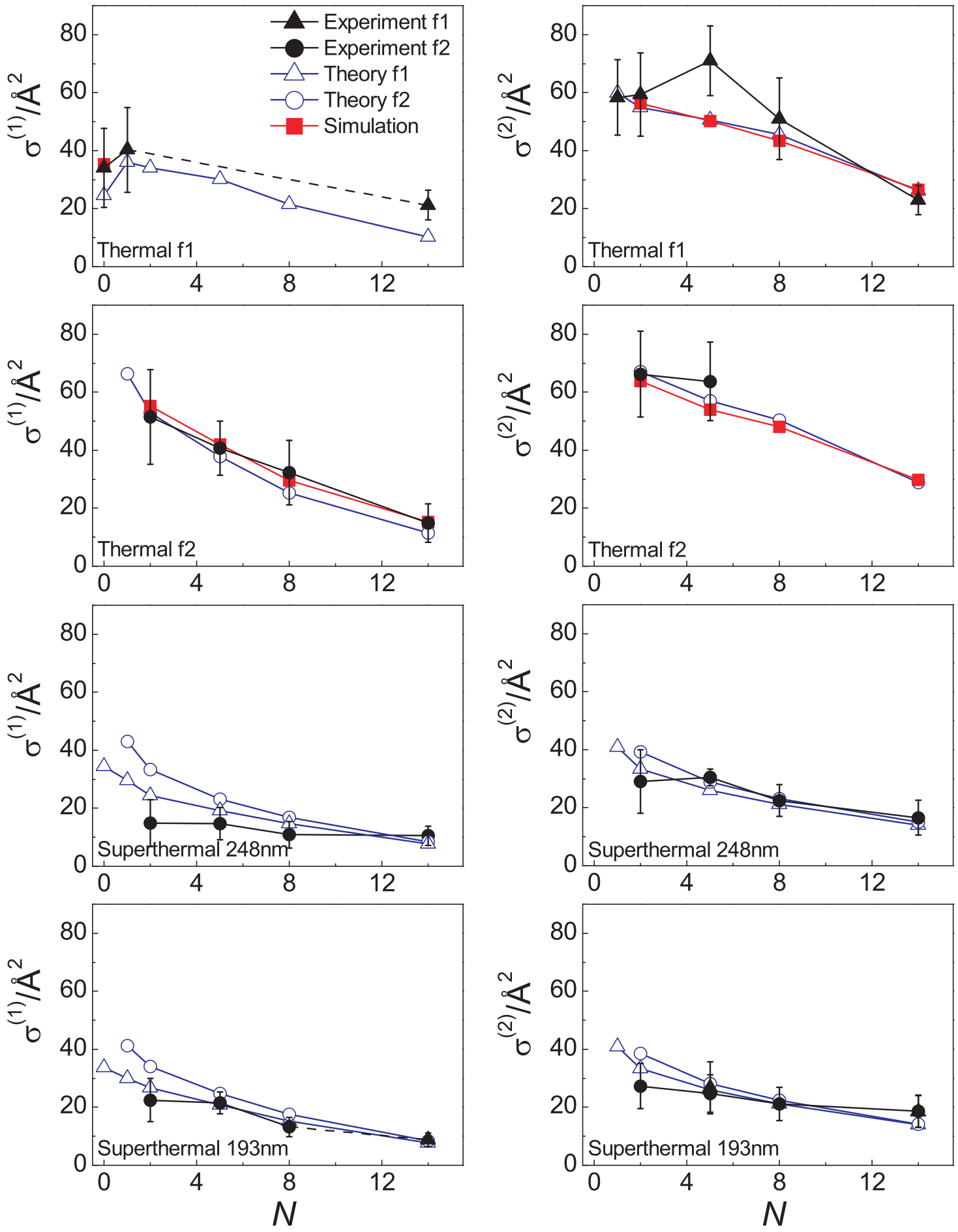
Experiment f1
Experiment f2
Theory f1
Theory f2
Simulation
Thermal f1
Thermal f2
Superthermal 248nm
Superthermal 193nm
σ(1)/Å2
σ(2)/Å2
N
0
20
40
60
80
0
4
8
12

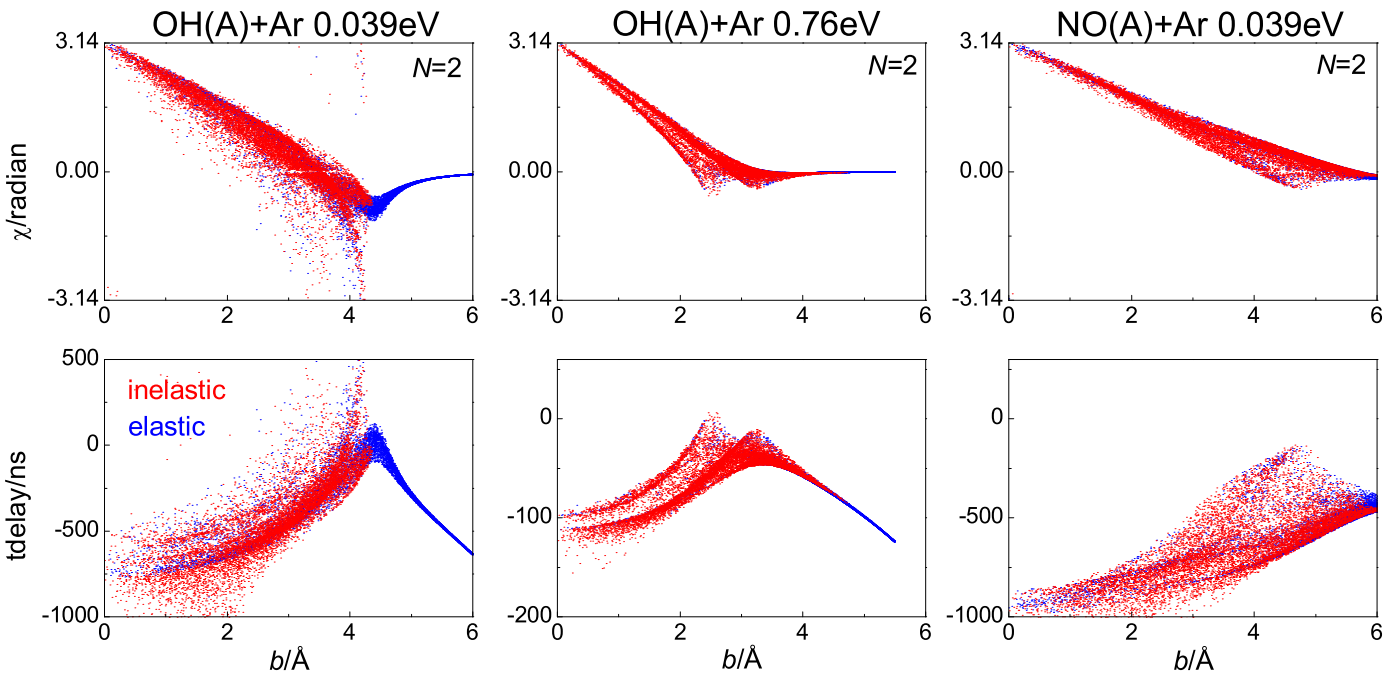
OH(A)+Ar 0.039eV
OH(A)+Ar 0.76eV
NO(A)+Ar 0.039eV
N=2
N=2
N=2
χ/radian
tdelay/ns
inelastic
elastic
b/Å
b/Å
b/Å

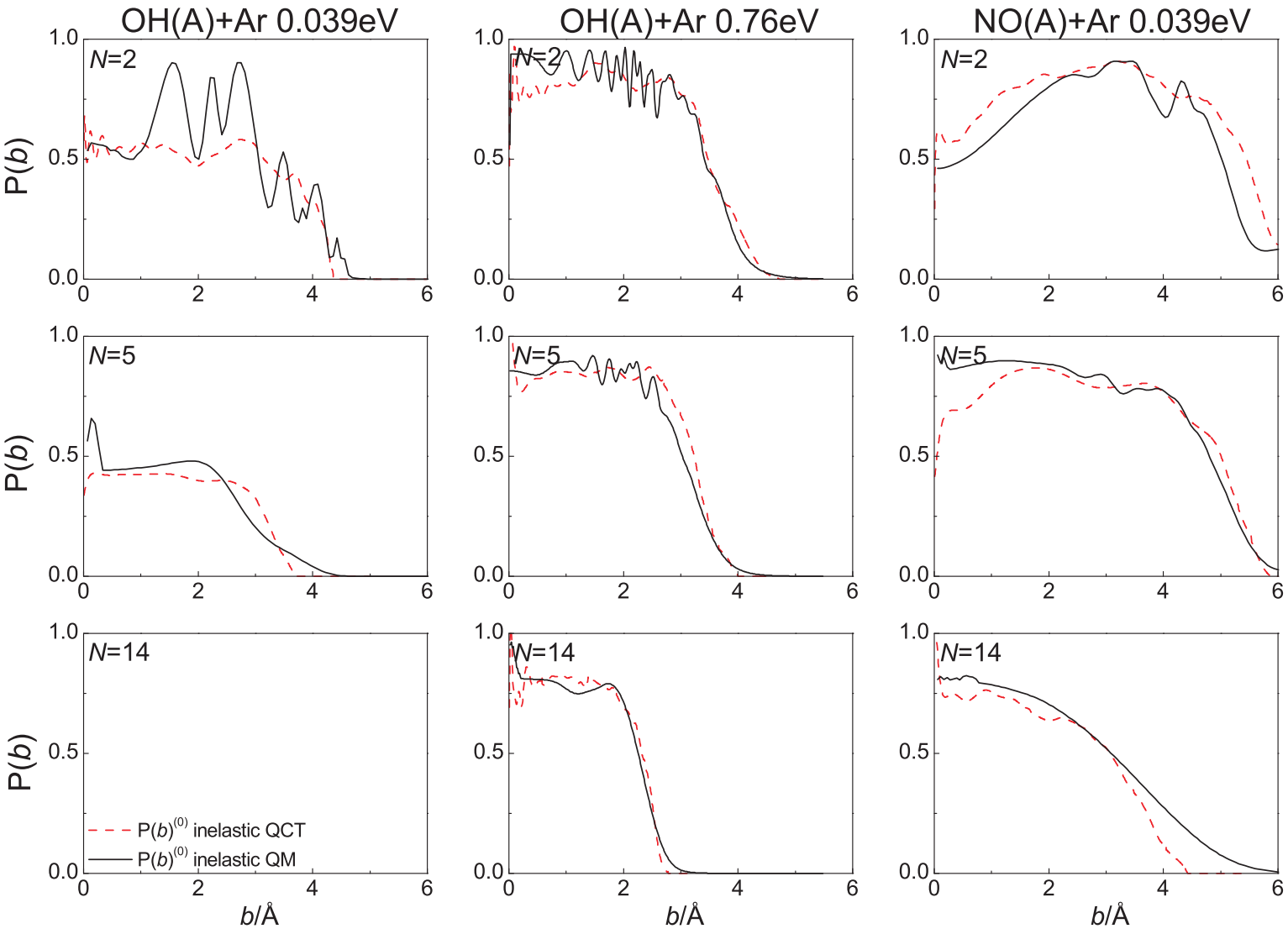
OH(A)+Ar 0.039eV
OH(A)+Ar 0.76eV
NO(A)+Ar 0.039eV
N=2
N=5
N=14
P(b)
b/Å
P(b)^(0) inelastic QCT
P(b)^(0) inelastic QM

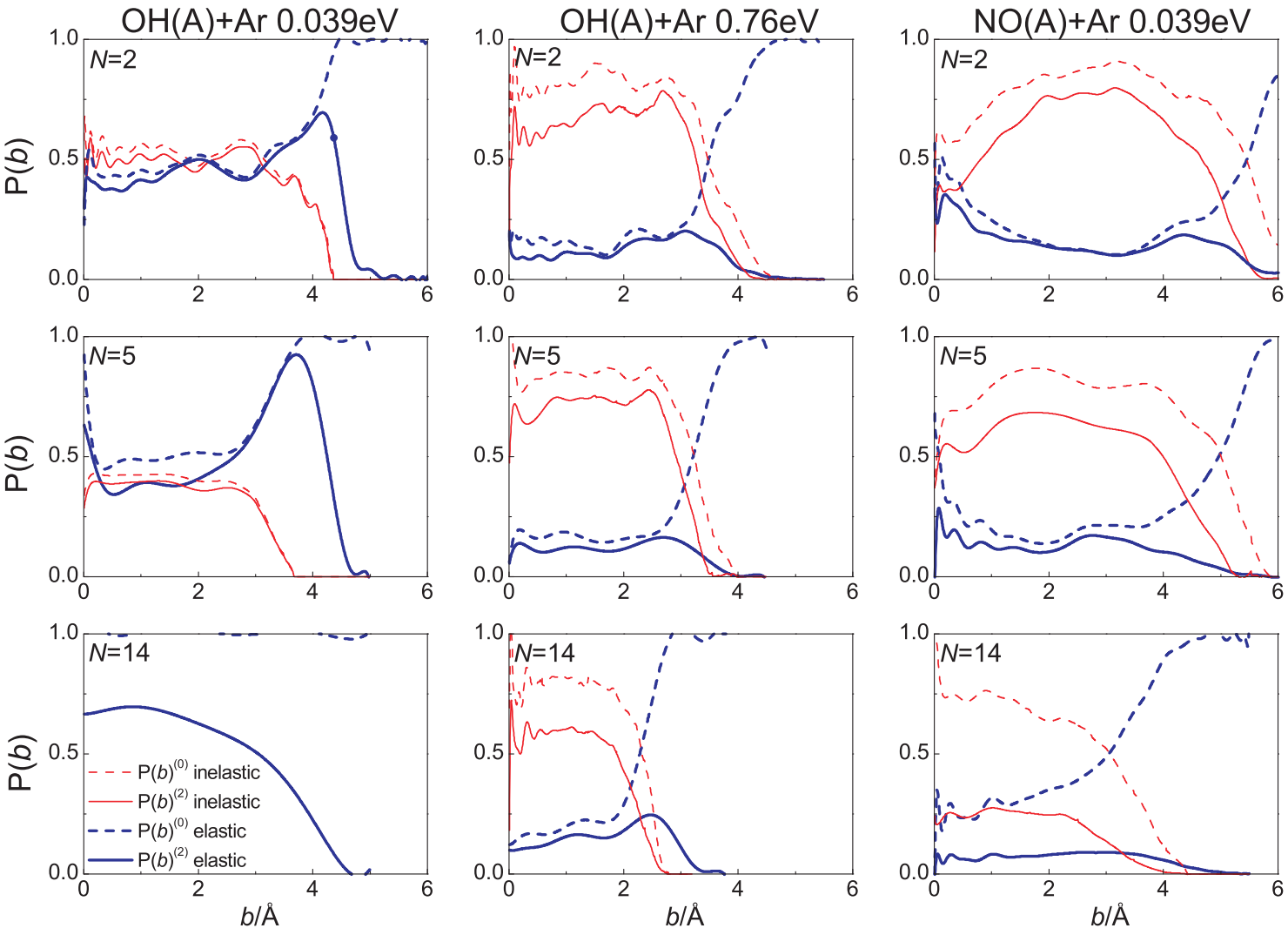
OH(A)+Ar 0.039eV
OH(A)+Ar 0.76eV
NO(A)+Ar 0.039eV
N=2
N=5
N=14
P(b)
b/Å
P(b)(0) inelastic
P(b)(2) inelastic
P(b)(0) elastic
P(b)(2) elastic

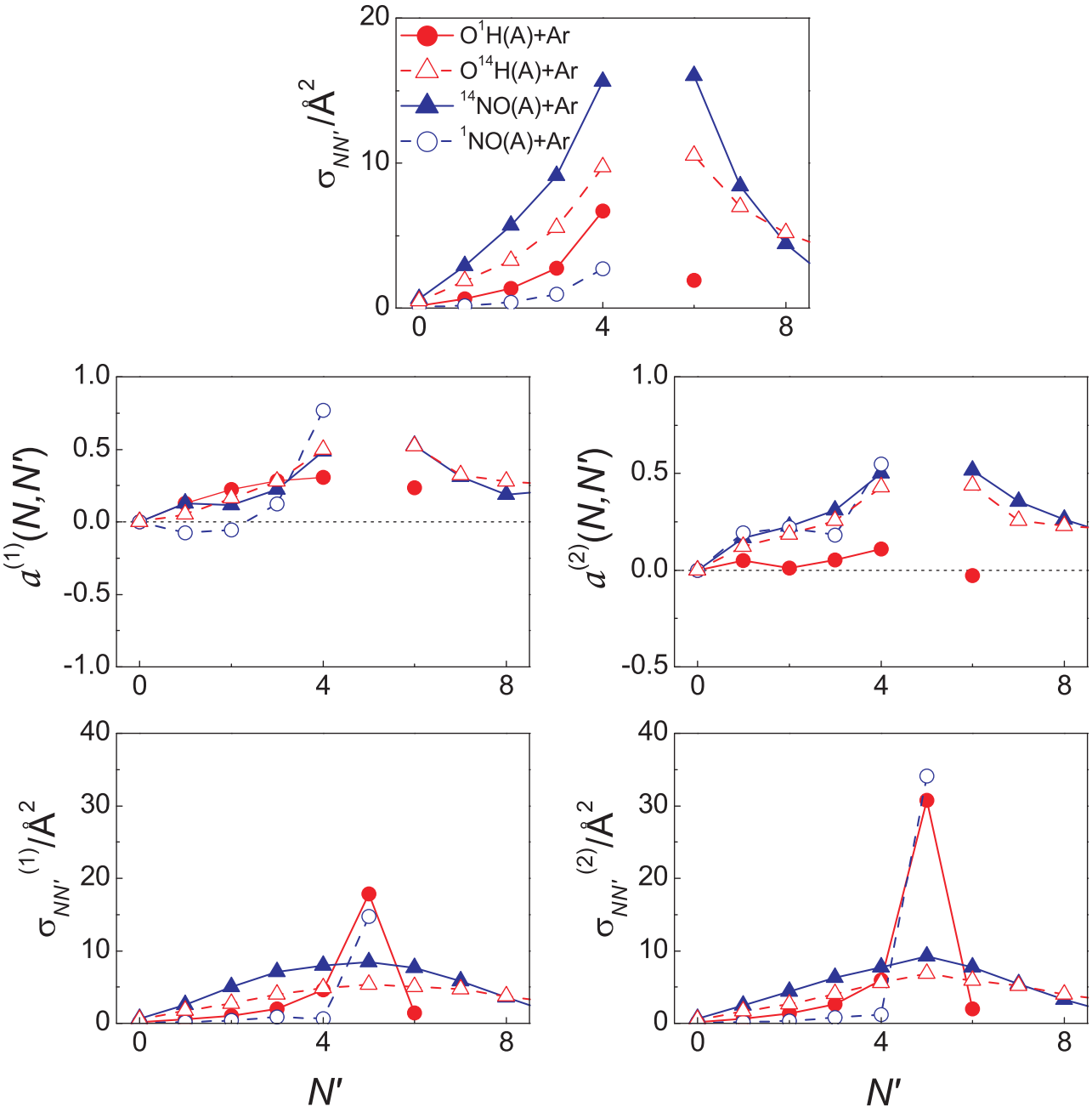
O1H(A)+Ar
O14H(A)+Ar
14NO(A)+Ar
1NO(A)+Ar
σNN'/Å2
a(1)(N,N')
a(2)(N,N')
σ(1)NN'/Å2
σ(2)NN'/Å2
N'

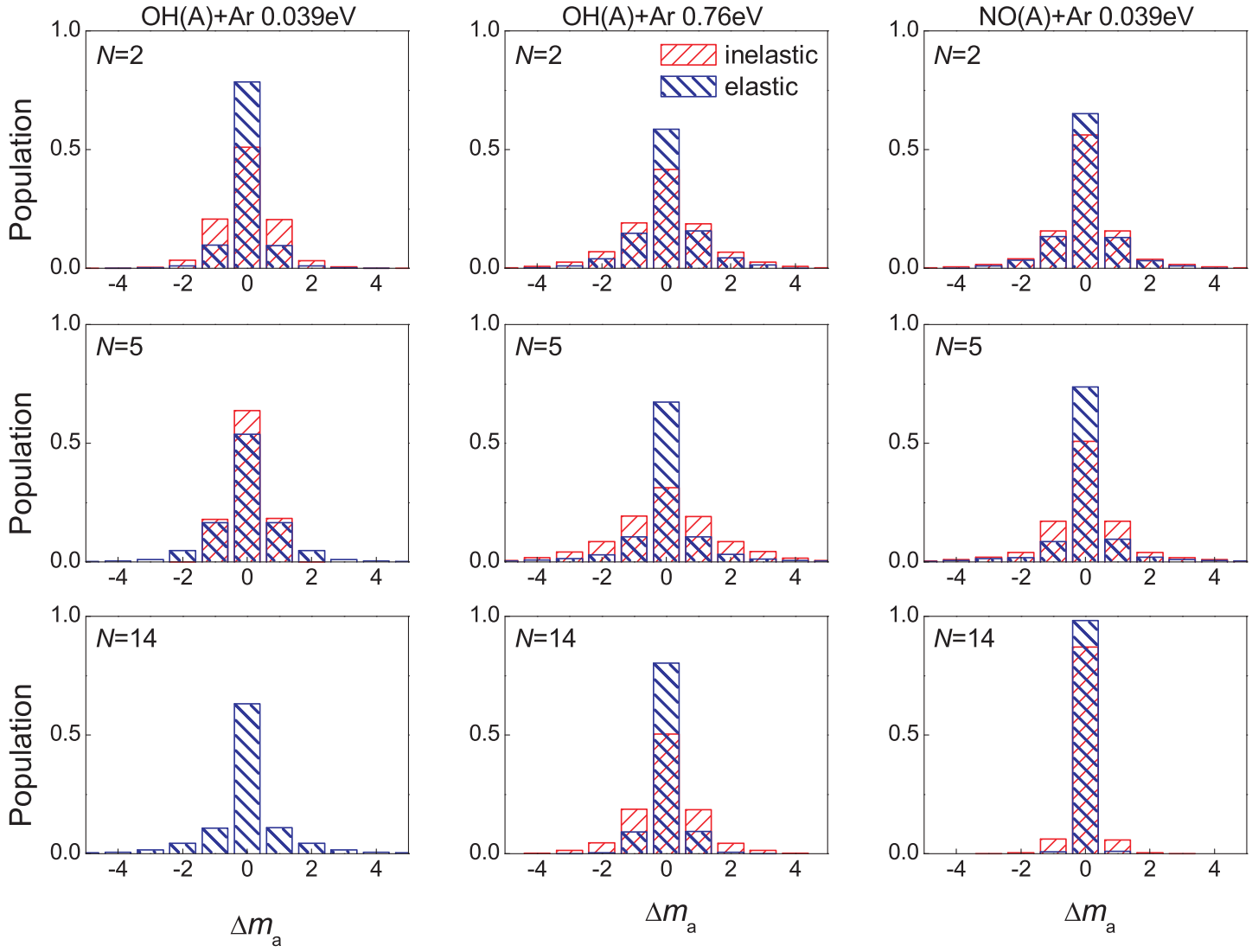
OH(A)+Ar 0.039eV
OH(A)+Ar 0.76eV
NO(A)+Ar 0.039eV
N=2
N=5
N=14
inelastic
elastic
Population
Δm_a
1.0
0.5
0.0
-4
-2
0
2
4

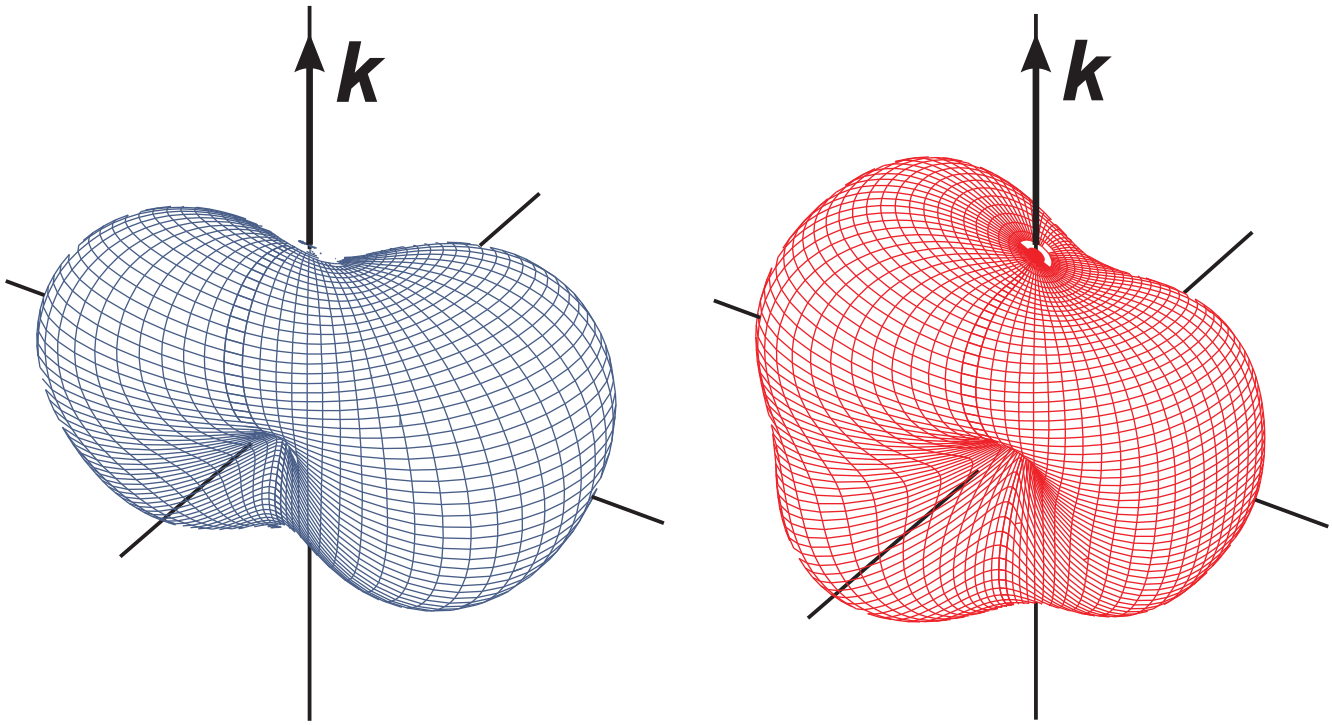
k
k

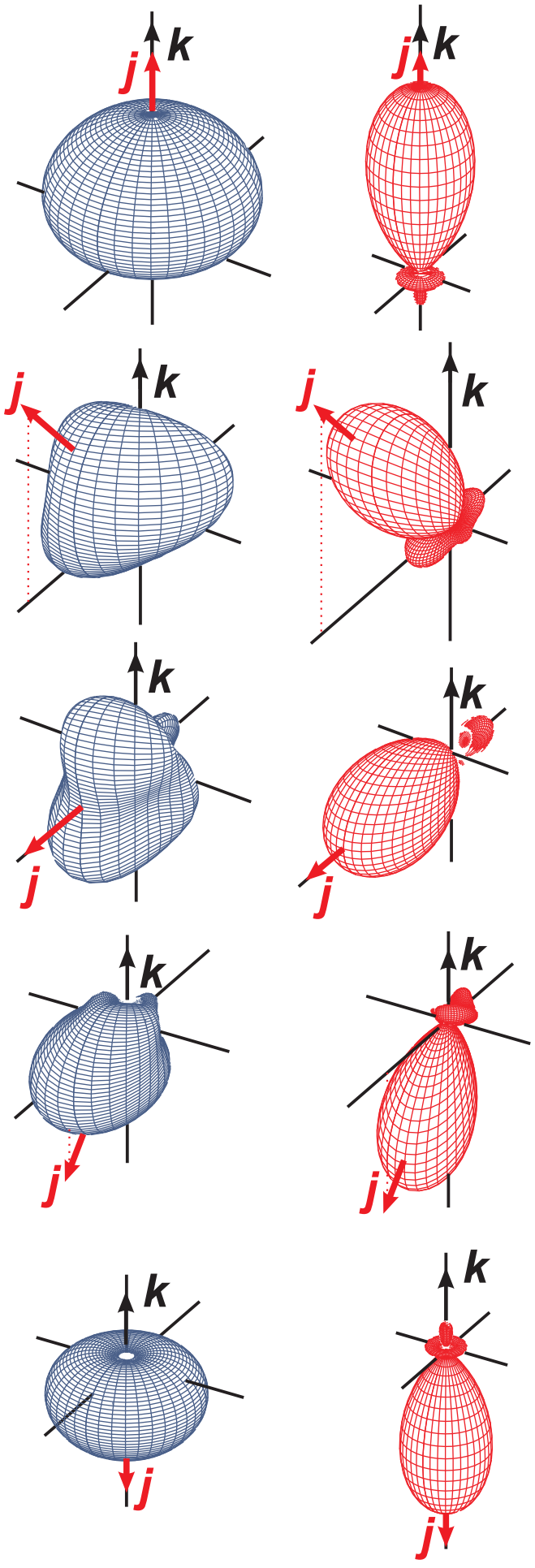
k
j
k
j
k
j
k
j
k
j
k
j
k
j
k
j
k
j
k
j

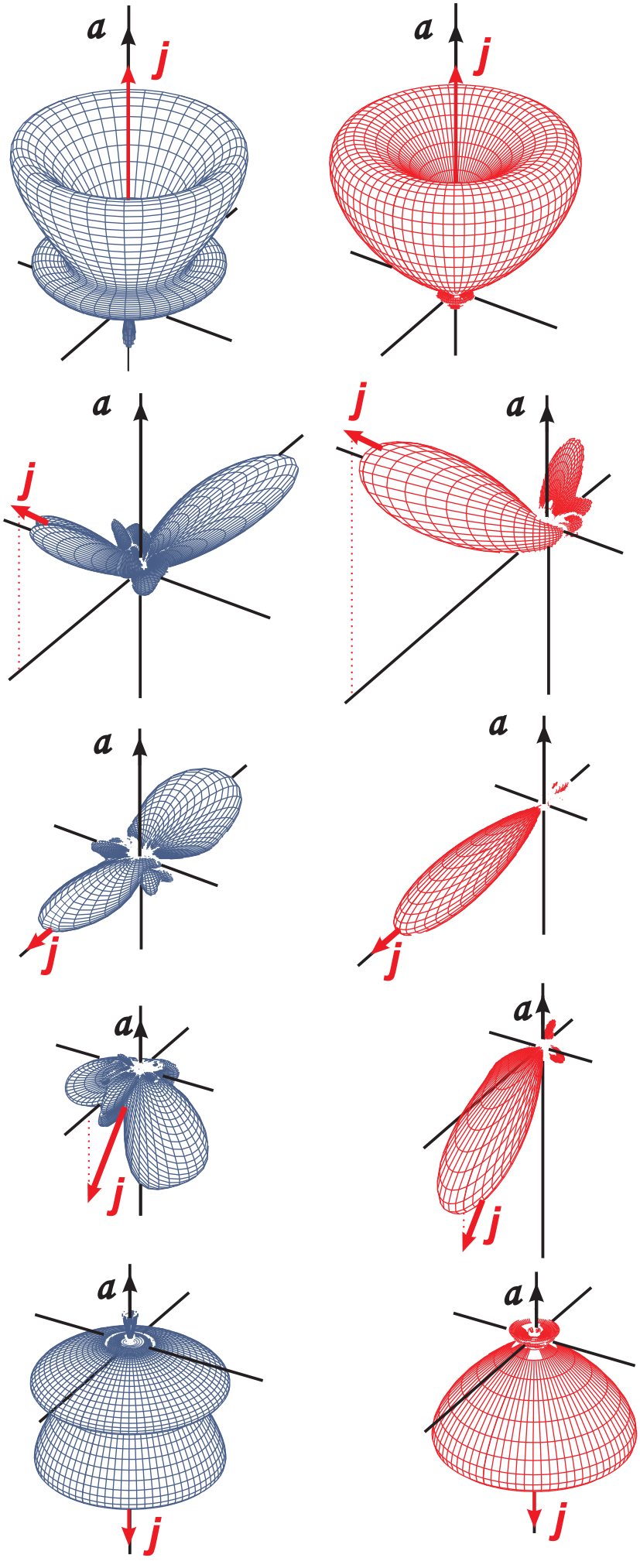
a
j
a
j
a
j
j
a
a
j
a
j
a
j
a
j
a
j
a
j